Bright-soliton frequency combs and dressed states in $\chi^{(2)}$ microresonators

D. N. Puzyrev, V. V. Pankratov, A. Villois, and D. V. Skryabin*
Department of Physics, University of Bath, Bath BA2 7AY, England, United Kingdom

(Received 13 May 2021; accepted 29 June 2021; published 19 July 2021)

We present a theory of frequency comb generation in high-Q ring microresonators with quadratic nonlinearity and normal dispersion and demonstrate that the naturally large difference of the repetition rates at the fundamental and second-harmonic frequencies supports a family of bright soliton frequency combs provided the parametric gain is moderated by tuning the index-matching parameter to exceed the repetition rate difference by a significant factor. This factor equals the sideband number associated with the high-order phase-matched sum-frequency process. The theoretical framework, i.e., the dressed-resonator method, to study the frequency conversion and comb generation is formulated by including the sum-frequency nonlinearity into the definition of the resonator spectrum. The Rabi splitting of the dressed frequencies leads to four distinct parametric down conversion conditions (signal-idler-pump photon energy conservation laws). The parametric instability tongues associated with the generation of the sparse, i.e., Turing-pattern-like, frequency combs with varying repetition rates are analyzed in detail. The sum-frequency matched sideband exhibits optical Pockels nonlinearity and strongly modified dispersion, which limit the soliton bandwidth and also play a distinct role in Turing comb generation. Our methodology and data highlight the analogy between the driven multimode resonators and the photon-atom interaction.

DOI: 10.1103/PhysRevA.104.013520

I. INTRODUCTION

Ring microresonators break through the traditional barriers of frequency conversion in terms of power efficiency, generated bandwidth, and compactness [1,2]. Together with the rise of microresonator frequency conversion, Kerr-soliton frequency combs are reaching unprecedented levels of practical relevance for optical solitons [1,2].

Second-order, $\chi^{(2)}$, nonlinearity is a viable alternative to the Kerr one. It provides a much stronger nonlinear response but comes with the caveat of the need to care about phase and group velocity matching to take full advantage of it. References [3–6] have been among the first ones to demonstrate frequency conversion in high-quality factor whispering gallery microresonators with quadratic nonlinearity. Since then, this area has made significant progress (see Ref. [7] for a few-years-old overview, and Refs. [8–15] for some more recent experimental contributions). It is also important to mention the work on $\chi^{(3)}$ dominant frequency conversion in significantly mismatched $\chi^{(2)}$ resonators (see, e.g., Refs. [16–19], and Appendix B for the relative weighting of the $\chi^{(2)}$ and $\chi^{(3)}$ effects). Materialwise, lithium-niobate remains the best-established platform choice for small-footprint $\chi^{(2)}$ photonics [8], with silicon [20] and aluminium [15] nitrides gaining ground with accelerating pace.

The whispering gallery system considered below achieves finesses $\mathcal{F} \sim 10^4$. The high finesse is an important prerequisite for achieving conditions when the rate of the sideband generating photon energy exchange driven by the sum-frequency nonlinear terms exceeds the loss rate [21,22] and the parametric gain rate [23], which corresponds to the strong-coupling (SC) regime between the ω and 2ω photons. As we have reported recently [23] and investigate in depth below, this makes the frequency conversion and soliton generation mechanisms depart significantly from what has been known about these effects in the relatively low finesse resonators, $\mathcal{F} \sim 10^2$, which often have no resonator feedback at one of the generated harmonics (see, e.g., Refs. [24,25] for an overview). A couple of the most obvious and important features of the high-$\mathcal{F}$ resonators are the channeling of the parametric gain into the tonguelike instability domains [23] and the strong coupling associated with the dressed states [21] and polaritons [23].

Experimental results on the $\chi^{(2)}$-driven microresonator solitons are limited for now by the outstanding recent report by Bruch and colleagues [15] on solitons due to parametric down conversion (PDC) in the aluminium-nitride microring with the finesse $\simeq 10^3$. The numerical data reported in Ref. [15] show the exponentially localized pulse in the half-harmonic field and the delocalized waveform in the pump. Reference [15] poses several problems, in particular, what are the physical mechanisms facilitating the compensation of the large group velocity (repetition rate) difference between the pump and half-harmonic fields allowing for the soliton to form; and whether a better shaped pulse in the pump field is possible. Identifying conditions for multicolor multipulse mode-locked solitons to compensate the large group velocity differences is one of the classic problems [26,27], that needs

*d.v.skryabin@bath.ac.uk

Published by the American Physical Society under the terms of the Creative Commons Attribution 4.0 International license. Further distribution of this work must maintain attribution to the author(s) and the published article's title, journal citation, and DOI.

to be addressed in the context of high-Q microresonators (see Ref. [28] for the no-resonator, i.e., bulk propagation, analysis).

Results on bright PDC solitons in the resonators with group velocity offset published two decades ago [27] provided a conceptual answer, that the compensation of the group velocity difference is achieved via the balancing interplay between the dissipative and nonlinear effects. However, Ref. [27] was published well before frequency combs and solitons in microresonators became possible. Therefore, it could not anticipate a combination of the small sizes and high Q-factors of modern day devices, which leads to the strong quantization of the spectra of the operators underpinning the frequency conversion and soliton formation processes. The model that fully reflects these aspects has been recently presented in Ref. [29], the introduction of which also includes sufficiently comprehensive coverage of recent and historical work on dissipative $\chi^{(2)}$ solitons in resonators.

Following our recent work on the theory of $\chi^{(2)}$ microresonators [12,23,29–31], we present here the latest findings obtained in the second-harmonic generation setting. One of the prime results included below is the demonstration of bright soliton pulses in a microresonator which has a large repetition rate difference between the fundamental, ω_p, and second-harmonic frequencies, $2\omega_p$ (see Sec. XIII).

The resonator considered here has a $\simeq$20-GHz repetition rate and a 1-GHz rate difference, which implies that the linear ω_p and $2\omega_p$ pulses would be on the opposite sides of the resonator only after about 70 round trips. The dispersion of the resonator is normal and its deviation from the bulk dispersion is insignificant. The dispersion value is $\simeq -100$ kHz so that the linear pulse becomes twice as broad after 10^5 round trips, and hence the repetition rate difference is by far the most dangerous for the bright soliton mode locking, which nevertheless will be shown to exist across a broad and practical range of system parameters.

The soliton combs reported below represent a pair of the ω_p and $2\omega_p$ mode-locked, and hence the repetition rate locked, bright pulses, the existence and properties of which are derived and interpreted by examining the details of how the comb teeth, i.e., the frequency sidebands, are generated and interact via the sum-frequency and PDC nonlinear mixing processes. The detailed understanding of this problem has become possible thanks to the dressed resonator theory [23]. The content of what follows is much wider than just reporting the soliton mode locking, and it is now useful to give it a brief overview.

II. CONTENT AND RESULTS OVERVIEW

The coupling between the sidebands, i.e., the resonator mode pairs or the comb teeth, underpins the formation of any frequency combs and mode locking in optical resonators. Below we consider microresonator second-harmonic generation, where the sideband coupling mechanisms embrace the complex interplay of the parametric process that couples the μ and $-\mu$ sidebands with the two sum-frequency processes. One is responsible for the coupling between the μ sidebands of the fundamental and second harmonic, while the other does the same but for the $-\mu$ sidebands. The sum-frequency processes can be phase matched for the select sidebands with the

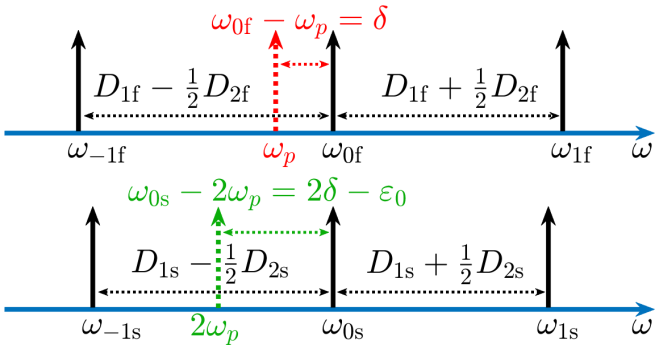

FIG. 1. A schematic illustration of the spectrum of the linear, i.e., bare, resonator, $\Omega = 0$, around the pump laser frequency, ω_p, and its second harmonic, $2\omega_p$. The frequency mismatch parameter ε_0 is tunable and could be comparable with $D_{1\zeta}$.

positive and negative numbers, $\mu = \mu_*$ or $\mu = -\mu_*$, where μ_* is the ratio between the phase-mismatch parameter and the repetition rate difference. The key resonator parameters and characteristics, including μ_*, are illustrated in Fig. 1, and defined in Tables I and II.

If the microresonator is tuned to operate away from the $\mu = 0$ phase matching, then the sum-frequency sideband coupling rate exceeds the parametric gain. It creates an opportunity to redefine the resonator spectrum by including the sum-frequency associated nonlinear terms. The new spectrum, i.e., the dressed spectrum, can be calculated analytically, bringing a close analogy with the dressing of the atomic transitions and the Rabi theory [21,23,32].

The condition of the maximal parametric gain [33–35],

$$2\hbar\omega_p = \hbar\omega_{\text{signal}} + \hbar\omega_{\text{idler}}, \tag{1}$$

should then be redefined using the dressed frequencies [23]. The Rabi splitting leads to four distinct PDC conditions [see Eq. (43)]. Knowing them allows understanding the complex structures of the parametric instability tongues and the Turing-pattern-like frequency combs across the parameter space spanned by the pump laser frequency, ω_p, and the intraresonator power.

The dressed modes around either μ_* or $-\mu_*$ exhibit dispersion with the inverted signs and the values significantly exceeding the bare-resonator ones. Therefore, only making μ_* sufficiently large, i.e., by taking it away from the soliton spectral core, creates enough of the modal bandwidth around $\mu = 0$ with the low dispersion allowing the formation of the two-color bright soliton pulses. The large values of μ_* are achieved by making the frequency mismatch parameter be-

TABLE I. The resonator parameters characteristic for a bulk-cut $LiNbO_3$ resonator pumped at 1065 nm [12,23,29]. $D_{2f,2s} < 0$ correspond to the normal dispersion.

Parameters	Values
Linewidths	$\kappa_f/2\pi = 1$ MHz, $\kappa_s/2\pi = 4$ MHz
Repetition rates	$D_{1f}/2\pi = 21$ GHz, $D_{1s}/2\pi = 20$ GHz
Dispersions	$D_{2f}/2\pi = -100$ kHz, $D_{2s}/2\pi = -200$ kHz
Nonlinear coefficients	$\gamma_{f,s}/2\pi = 300$ MHz$/\sqrt{\text{W}}$

TABLE II. Definitions of the key parameters, which complement the ones illustrated in Fig. 1 and listed in Table I. ω_p is the laser photon frequency. $\omega_{\mu\zeta}$ and $\widetilde{\omega}_{\mu\zeta}^{(j)}$ are the bare and dressed resonator frequencies, respectively ($j_{1,2} = 1, 2, 3, 4$; $\zeta = f, s$).

Parameters	Values
Rabi frequency	$\Omega = \psi_{0\mathrm{f}}\sqrt{8\gamma_\mathrm{f}\gamma_\mathrm{s}}$ $\approx \psi_{0\mathrm{f}} \times 0.8\ \mathrm{GHz}/\sqrt{\mathrm{W}}$
Rabi detuning	$\Delta_\mu = \omega_p + \omega_{\mu\mathrm{f}} - \omega_{\mu\mathrm{s}}$
Sum-frequency mismatch	$\varepsilon_\mu = \omega_{0\mathrm{f}} + \omega_{\mu\mathrm{f}} - \omega_{\mu\mathrm{s}}$
Effective Rabi frequency	$\Omega_\mu = \sqrt{\Delta_\mu^2 + \lvert\Omega\rvert^2}$
PDC frequency mismatch	$\varepsilon_\mu^{(j_1 j_2)} = \widetilde{\omega}_{\mu\mathrm{f}}^{(j_1)} + \widetilde{\omega}_{-\mu\mathrm{f}}^{(j_2)} - 2\omega_p$
Strong-coupling condition	$\kappa_\zeta \ll \lvert\Omega\rvert \ll 8\lvert\varepsilon_0\rvert$
Sum-frequency matching	$\varepsilon_{\pm\mu_*} = 0,\ \mu_* \approx \lvert\varepsilon_0\rvert/\lvert D_{1\mathrm{f}} - D_{1\mathrm{s}}\rvert$

tween the fundamental and second-harmonic modes exceed the repetition rate difference by a significant, $\gg 1$, factor, which works out to be μ_* itself. Now, we are proceeding with the details of the theoretical and numerical results.

III. LINEARIZED SIDEBAND EQUATIONS AND CW STATE

We assume the intraresonator electric fields of the fundamental and second harmonic to be

$$\psi_\mathrm{f} e^{iM\vartheta - i\omega_p t} + \mathrm{c.c.},\ \psi_\mathrm{s} e^{i2M\vartheta - i2\omega_p t} + \mathrm{c.c.}, \tag{2}$$

where $|\psi_{\mathrm{f,s}}|^2$ have units of power [29] (see Appendix A). M and $2M$ are the absolute (physical) mode numbers with frequencies $\omega_{0\mathrm{f}}$ and $\omega_{0\mathrm{s}}$. $\vartheta \in (-\pi, \pi]$ is the angular coordinate and t is time. ω_p is the pump laser frequency tunable around $\omega_{0\mathrm{f}}$, so that

$$\delta = \omega_{0\mathrm{f}} - \omega_p \tag{3}$$

is the respective pump detuning.

The envelopes of the fundamental, ψ_f, and second harmonic, ψ_s, are expressed via their mode expansions as

$$\psi_\zeta = \psi_{0\zeta}(t) + \sum_{\mu>0}[\psi_{\mu\zeta}(t)e^{i\mu\vartheta} + \psi_{-\mu\zeta}(t)e^{-i\mu\vartheta}], \tag{4}$$

with $\zeta = f, s$, and μ is an integer characterizing the relative mode number. The resonator frequencies associated with $\psi_{\pm\mu\zeta}$ are

$$\omega_{\pm\mu\zeta} = \omega_{0\zeta} \pm \mu D_{1\zeta} + \tfrac{1}{2}\mu^2 D_{2\zeta}, \tag{5}$$

where $D_{1\zeta}/2\pi$ are the repetition rates (free spectral ranges) and $D_{2\zeta}$ are the dispersions (see Fig. 1 for a schematic illustration). The photon angular momenta corresponding to $\omega_{\pm\mu\mathrm{f}}$ and $\omega_{\pm\mu\mathrm{s}}$ are

$$\hbar(M \pm \mu),\ \text{and}\ \hbar(2M \pm \mu).$$

Physical values of the parameters implemented throughout this paper are shown in Table I, and are typical for a bulk-cut $LiNbO_3$ resonator. Detunings of the resonator frequencies $\omega_{\pm\mu\zeta}$ from the pump laser frequency, ω_p, and its second harmonic, $2\omega_p$, are $\omega_{\pm\mu\mathrm{f}} - \omega_p$ and $\omega_{\pm\mu\mathrm{s}} - 2\omega_p$. A Galilean transformation to the reference frame rotating with the rate $D_1/2\pi$,

$$\theta = \vartheta - D_1 t, \tag{6}$$

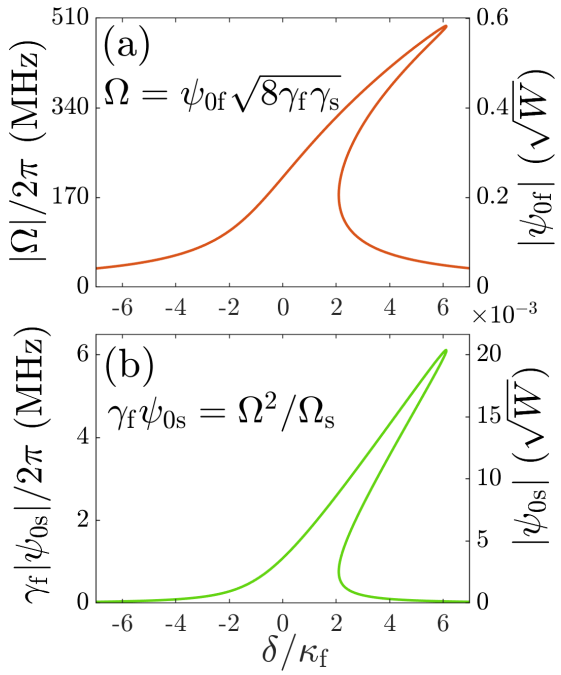

FIG. 2. Cw state of the (a) fundamental and (b) second harmonic (see Appendix C). Pump laser power is $\mathcal{W} = 0.1$ mW [see Eq. (49)]. Mismatch parameter $\varepsilon_0/2\pi = -5$ GHz.

converts these detunings to

$$\begin{aligned}\Delta_{\pm\mu\mathrm{f}} &= (\omega_{\pm\mu\mathrm{f}} - \omega_p) \mp \mu D_1 \\ &= \delta \pm \mu(D_{1\mathrm{f}} - D_1) + \tfrac{1}{2}D_{2\mathrm{f}}\mu^2, \\ \Delta_{\pm\mu\mathrm{s}} &= (\omega_{\pm\mu\mathrm{s}} - 2\omega_p) \mp \mu D_1 \\ &= 2\delta - \varepsilon_0 \pm \mu(D_{1\mathrm{s}} - D_1) + \tfrac{1}{2}D_{2\mathrm{s}}\mu^2,\end{aligned} \tag{7}$$

where $\varepsilon_0 = 2\omega_{0\mathrm{f}} - \omega_{0\mathrm{s}}$ is the $\mu = 0$ frequency mismatch parameter. Setting

$$D_1 = D_{1\mathrm{f}}, \tag{8}$$

we get an immediate access to the difference of the repetition rates, $D_{1\mathrm{s}} - D_{1\mathrm{f}}$, inside $\Delta_{\pm\mu\mathrm{s}}$.

If c is the vacuum speed of light, $n_{M+\mu}$ is the effective refractive index of the mode $M + \mu$, and R is the resonator radius, then

$$\omega_{\mu\mathrm{f}} = \frac{c}{R}\frac{(M+\mu)}{n_{M+\mu}},\ \omega_{\mu\mathrm{s}} = \frac{c}{R}\frac{(2M+\mu)}{n_{2M+\mu}}. \tag{9}$$

Hence,

$$\varepsilon_0 = 2\omega_{0\mathrm{f}} - \omega_{0\mathrm{s}} = 2M\frac{c}{R}\left[\frac{1}{n_M} - \frac{1}{n_{2M}}\right], \tag{10}$$

and requiring $\varepsilon_0 = 0$, yields the anticipated index matching condition, $n_M = n_{2M}$. Refractive index, and hence ε_0, can be fine tuned by, e.g., temperature or electro-optic controls.

The cw state of the resonator operation implies $\psi_\zeta = \psi_{0\zeta} = \mathrm{const}_\zeta$, i.e., $\partial_t \psi_{0\zeta} = 0$ (see Fig. 2 and Appendix C). During the initial stage of the comb development, the sidebands evolve and grow on top of the undepleted cw state, so that the field envelopes can be sought as the cw plus small perturbations, with the latter taken as a superposition of the

resonator modes:

$$\psi_\zeta(t,\theta) = \psi_{0\zeta} + \sum_{\mu\geqslant 0}[\widetilde{\psi}_{\mu\zeta}(t)e^{i\mu\theta} + \widetilde{\psi}^*_{-\mu\zeta}(t)e^{-i\mu\theta}]. \quad (11)$$

Here $\widetilde{\psi}_{\pm\mu\zeta}$ are the amplitudes of the growing sidebands. Complex conjugation of $\widetilde{\psi}_{-\mu\zeta}$ was introduced to make the equations less cluttered. If Eq. (4) could be referred to as the mode expansion in the bare resonator representation, then Eq. (11) is a step towards the dressed resonator theory.

Substituting Eq. (11) into the envelope equations (A1), and linearizing for small sidebands, we find that $\widetilde{\psi}_{\mu\zeta}(t)$ are driven by the sideband combinations with the matched net momenta (see Appendix D). The resulting equations are

$$\begin{aligned}
i\partial_t\widetilde{\psi}_{\mu\mathrm{f}} &= \left(\Delta_{\mu\mathrm{f}} - i\frac{1}{2}\kappa_\mathrm{f}\right)\widetilde{\psi}_{\mu\mathrm{f}} - \gamma_\mathrm{f}(\underline{\widetilde{\psi}_{\mu\mathrm{s}}\psi^*_{0\mathrm{f}}} + \underline{\underline{\widetilde{\psi}_{-\mu\mathrm{f}}\psi_{0\mathrm{s}}}}),\\
i\partial_t\widetilde{\psi}_{\mu\mathrm{s}} &= \left(\Delta_{\mu\mathrm{s}} - i\frac{1}{2}\kappa_\mathrm{s}\right)\widetilde{\psi}_{\mu\mathrm{s}} - 2\gamma_\mathrm{s}\underline{\widetilde{\psi}_{\mu\mathrm{f}}\psi_{0\mathrm{f}}},\\
i\partial_t\widetilde{\psi}_{-\mu\mathrm{f}} &= \left(-\Delta_{-\mu\mathrm{f}} - i\frac{1}{2}\kappa_\mathrm{f}\right)\widetilde{\psi}_{-\mu\mathrm{f}} + \gamma_\mathrm{f}(\underline{\widetilde{\psi}_{-\mu\mathrm{s}}\psi_{0\mathrm{f}}} + \underline{\underline{\widetilde{\psi}_{\mu\mathrm{f}}\psi^*_{0\mathrm{s}}}}),\\
i\partial_t\widetilde{\psi}_{-\mu\mathrm{s}} &= \left(-\Delta_{-\mu\mathrm{s}} - i\frac{1}{2}\kappa_\mathrm{s}\right)\widetilde{\psi}_{-\mu\mathrm{s}} + 2\gamma_\mathrm{s}\underline{\widetilde{\psi}_{-\mu\mathrm{f}}\psi^*_{0\mathrm{f}}}. \qquad (12)
\end{aligned}$$

Here, κ_ζ are the loaded linewidth parameters, and γ_ζ are the nonlinear coefficients measured in $\mathrm{Hz/W}^{1/2}$ [29] (see Table I).

Equations (12) are linear in the approximation of the undepleted cw state, and they represent one of the fundamental models in nonlinear optics expressing the interplay of the PDC and sum-frequency processes. The sum-frequency terms are underlined once and the parametric ones, describing conversion to the $\pm\mu$ sidebands (photon-pair generation), are underlined twice. The momentum conservation laws corresponding to the parametric conversion and the two sum-frequency processes are

$$\hbar(M+\mu) + \hbar(M-\mu) = \hbar 2M \quad (13)$$

and

$$\hbar(M\pm\mu) + \hbar M = \hbar(2M\pm\mu), \quad (14)$$

respectively.

The eigenvalues and eigenvectors of the matrix acting on the vector $(\widetilde{\psi}_{\mu\mathrm{f}}, \widetilde{\psi}_{\mu\mathrm{s}}, \widetilde{\psi}_{-\mu\mathrm{f}}, \widetilde{\psi}_{-\mu\mathrm{s}})^T$ in the right-hand side of Eq. (12) are known in the explicit form in two cases: (i) for $\Delta_{\mu\mathrm{f}} = \Delta_{-\mu\mathrm{f}}$, $\Delta_{\mu\mathrm{s}} = \Delta_{-\mu\mathrm{s}}$, and $\kappa_\mathrm{f} = \kappa_\mathrm{s}$ (see, e.g., Refs. [36–38]) and (ii) for $\kappa_\mathrm{f} \neq \kappa_\mathrm{s}$ and $\Delta_{\pm\mu\zeta} = 0$ (see Ref. [39]). While $\Delta_{\mu\mathrm{f}} = \Delta_{-\mu\mathrm{f}}$ is satisfied exactly, and $\kappa_\mathrm{f} = \kappa_\mathrm{s}$ could be assumed, the $\Delta_{\mu\mathrm{s}} = \Delta_{-\mu\mathrm{s}}$ condition is typically far from being true. In most of the practical cases, the repetition rate difference, $\Delta_{\mu\mathrm{s}} - \Delta_{-\mu\mathrm{s}} = 2\mu(D_{1\mathrm{s}} - D_{1\mathrm{f}})$, creates one of the dominant frequency scales in Eqs. (7), which can be comparable only to ε_0.

IV. RABI FREQUENCY, PARAMETRIC GAIN, AND LINEWIDTH

To address the problem at hand, it is important to understand the balances between the characteristic frequency scales implicated in Eq. (12). $\psi_{0\mathrm{s}}$, i.e., the cw second-harmonic amplitude, can be controlled by tuning the frequency mismatch, ε_0, so that the parametric gain coefficient, $\gamma_\mathrm{f}\psi_{0\mathrm{s}}$, can be made to be much less than the sum-frequency associated rate of the energy exchange, $\gamma_\zeta\psi_{0\mathrm{f}}$ (see Fig. 2 and compare the frequency scales along the vertical axes).

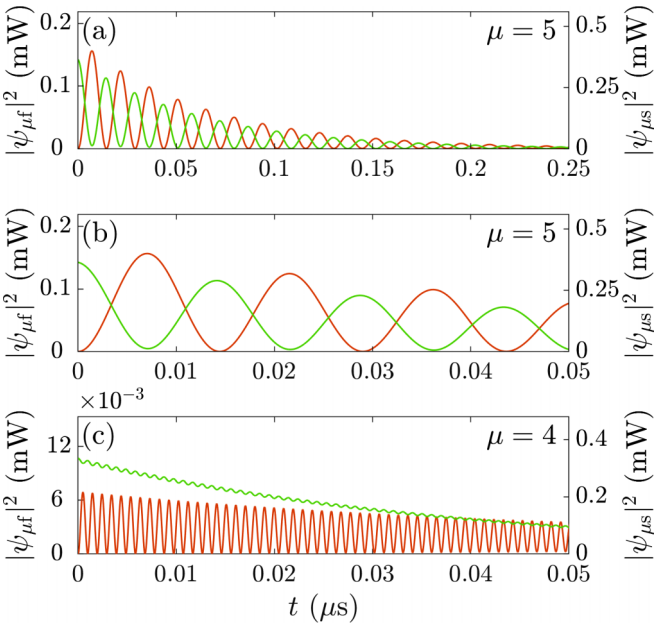

FIG. 3. (a) The sum-frequency matched Rabi oscillations near to the $\mu = 5$ avoided crossing (red, fundamental, left axis; green, second harmonic, right axis), $\Omega_5 \approx |\Omega| \approx 2\pi \times 68$ MHz. (b) As in (a) but plotted over the time interval as is used in (c). (c) The mismatched Rabi oscillations for the $\mu = 4$ sidebands, $\Omega_4 \approx |\Delta_4| \approx 2\pi \times 1$ GHz. Parameters: (a, b) $\delta = 15.15\kappa_\mathrm{f}$, $\varepsilon_0/2\pi = -5$ GHz, $\mathcal{W} = 1.7$ mW (pump power), $|\psi_{5\mathrm{s}}|^2 = 0.36$ mW (sideband power) at $t = 0$; (c) $\delta = 6.45\kappa_\mathrm{f}$, $\varepsilon_0/2\pi = -5$ GHz, $\mathcal{W} = 2.11$ mW, $|\psi_{4\mathrm{s}}|^2 = 0.33$ mW at $t = 0$.

If the aim is to create the modal bandwidth sufficient for the soliton generation at both harmonics, then the moderation of the parametric gain is useful since it would then keep the energy of the second-harmonic pulse under control, and, hence, could be expected to ease, for the stronger fundamental pulse, the task of synchronizing its repetition rate with the second harmonic.

The sum-frequency driven energy exchange is illustrated in Fig. 3, where one can see the fast antiphase oscillations of the $\omega_{\mu\mathrm{f}}$ and $\omega_{\mu\mathrm{s}}$ sidebands. The frequency of the oscillations is much larger than the decay rates, so that, in the leading order, the first two equations in Eqs. (12) can be approximated with [23,40]

$$i\partial_t\begin{bmatrix}\widetilde{\psi}_{\mu\mathrm{f}}\\ \widetilde{\psi}_{\mu\mathrm{s}}\end{bmatrix} \approx \begin{bmatrix}\Delta_{\mu\mathrm{f}} & -\gamma_\mathrm{f}\psi^*_{0\mathrm{f}}\\ -2\gamma_\mathrm{s}\psi_{0\mathrm{f}} & \Delta_{\mu\mathrm{s}}\end{bmatrix}\begin{bmatrix}\widetilde{\psi}_{\mu\mathrm{f}}\\ \widetilde{\psi}_{\mu\mathrm{s}}\end{bmatrix} + \ldots. \quad (15)$$

The second pair of equations resembles the above but with $\mu \to -\mu$. Parametric gain and losses should then come in the next to leading order, suggesting the development of a perturbation theory. The Rabi theory, well known in the semiclassical atom-photon interaction [32], is an obvious and best suited methodology to describe solutions of Eq. (15). The Rabi formalism was also previously applied for the resonator-free sum-frequency generation model [41].

The frequency of the oscillations in Fig. 3 would then be the effective Rabi frequency:

$$\Omega_\mu = \sqrt{\Delta_\mu^2 + |\Omega|^2}. \tag{16}$$

It is controlled by the difference of the sideband detunings, i.e., the Rabi detuning,

$$\Delta_\mu = \Delta_{\mu\mathrm{f}} - \Delta_{\mu\mathrm{s}}, \tag{17}$$

and by the coupling coefficient, i.e., by the off-diagonal terms in Eq. (15), characterized by the complex Rabi frequency, Ω:

$$\Omega = \psi_{0\mathrm{f}}\sqrt{8\gamma_\mathrm{f}\gamma_\mathrm{s}}. \tag{18}$$

The complex second-harmonic amplitude can also be expressed via Ω and the auxiliary complex frequency Ω_s:

$$\gamma_\mathrm{f}\psi_{0\mathrm{s}} = \frac{\Omega^2}{\Omega_\mathrm{s}},\ \Omega_\mathrm{s} = 8\left(2\delta - i\frac{1}{2}\kappa_\mathrm{s}\right) - 8\varepsilon_0 \tag{19}$$

(see Appendix C).

$|\Omega|/2\pi \sim 10^2$ MHz gives $|\psi_{0\mathrm{f}}|^2 \lesssim 1$W, which would be typical inside the resonator. Then, for $\kappa_\zeta/2\pi \sim 1$ MHz we have $|\Omega| \gg \kappa_\zeta$, i.e., the Rabi flops are indeed much faster than the decay rate. The frequency scale associated with the parametric gain is set by

$$\gamma_\mathrm{f}|\psi_{0\mathrm{s}}| = \frac{|\Omega|^2}{|\Omega_\mathrm{s}|}. \tag{20}$$

Arranging $|\varepsilon_0|$ to be close to or larger than the repetition rate difference,

$$\frac{|\varepsilon_0|}{2\pi} \gtrsim \frac{|D_{1\mathrm{f}} - D_{1\mathrm{s}}|}{2\pi} \simeq 1\ \mathrm{GHz}, \tag{21}$$

makes

$$\frac{1}{|\Omega|}\frac{|\Omega|^2}{|\Omega_\mathrm{s}|} \approx \frac{|\Omega|}{8|\varepsilon_0|} \ll 1. \tag{22}$$

Hence, the Rabi frequency is also much larger than the parametric gain rate. Thus, both the linewidth and the parametric terms are small relative to the right-hand side of Eq. (15), and the SC condition [23],

$$\kappa_\zeta \ll |\Omega| \ll |\Omega_\mathrm{s}|, \tag{23}$$

is satisfied. Reference [21] reported measurements of the $\chi^{(2)}$ Rabi splitting ($\approx$1 GHz for the laser power $\mathcal{W} = 80$ mW) in the AlN resonators with $|\Omega|/\kappa_\zeta \sim 1$, which should be well outperformed by the bulk resonators considered here. The $\mu = 0$ Rabi oscillations in the $\chi^{(2)}$ resonators were looked at in Ref. [42], well before the multimode high-Q $\chi^{(2)}$ microresonators were demonstrated.

The notations related to the Rabi theory and also the key quantities used below to characterize the matching conditions for the sum-frequency and parametric processes are summarized in Table II.

V. SUM-FREQUENCY MATCHING

While the cascade of the sum- and difference-frequency events engaging a sequence of μ's is critical for the generation of the fully blown combs (see Sec. X), the frequency matching for the one-step sum-frequency process in Eq. (13) is also very important and should be analyzed in more details. As it is well known for the coupled oscillators, the full periodic power transfer between $\widetilde{\psi}_{\mu\mathrm{f}}$ and $\widetilde{\psi}_{\mu\mathrm{s}}$ is ensured by minimizing the Rabi detuning, i.e., $\Delta_\mu \to 0$, $\Omega_\mu \to |\Omega|$ [see Eq. (16)].

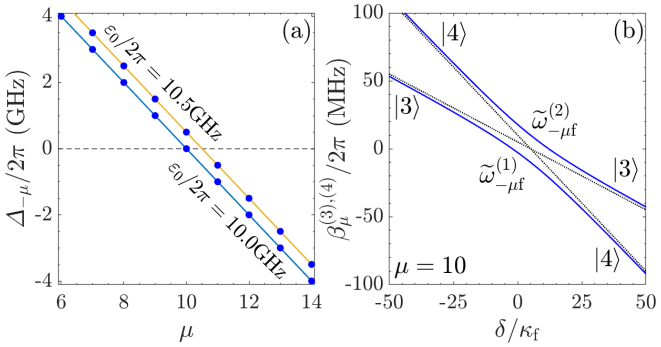

FIG. 4. (a) Frequency matching for the sum-frequency generation: The Rabi detuning $\Delta_{-\mu} = \omega_p + \omega_{-\mu\mathrm{f}} - \omega_{-\mu s}$ vs the sideband order number μ, $\delta = 5\kappa_\mathrm{f}$. $\varepsilon_0/2\pi = 10.5$ and 10 GHz correspond to the mismatched and near-matched ($\mu = \widehat{\mu} = 10$) cases, respectively. (b) Avoided-crossing diagram: The dressed frequencies vs δ for $|\Omega| = 20\kappa_\mathrm{f}$. The straight lines correspond to $\Omega = 0$.

Here, we are dealing with a system possessing two different effective Rabi frequencies Ω_μ and $\Omega_{-\mu}$, and the respective Rabi detunings, $\Delta_{\pm\mu}$, can be reexpressed as

$$\Delta_{\pm\mu} = \omega_p + \omega_{\pm\mu\mathrm{f}} - \omega_{\pm\mu\mathrm{s}}. \tag{24}$$

If one of $\Delta_{\pm\mu} = 0$ is resolved by an integer, i.e.,

$$\Delta_{\widehat{\mu}} = 0,\ \text{or}\ \Delta_{-\widehat{\mu}} = 0,\ \widehat{\mu} \in \mathbb{Z},\ \widehat{\mu} > 0, \tag{25}$$

it implies the exact matching for one of the two coexisting sum-frequency processes. The examples of the exact matching between $\omega_{-\mu\mathrm{f}}$ and $\omega_{-\mu\mathrm{s}}$ for $\mu = 10$ and of the mismatched case are shown in Fig. 4(a). In the mismatched case, the SC condition, Eq. (23), is perfectly satisfied, but the power transfer during the Rabi flops is significantly reduced [see Figs. 3(b) and 3(c)].

If the real positive μ_* solves one of the $\Delta_{\pm\mu} = 0$ equations, i.e.,

$$\Delta_{\mu_*} = 0,\ \text{or}\ \Delta_{-\mu_*} = 0,\ \mu_* \in \mathbb{R},\ \mu_* > 0, \tag{26}$$

then an integer, or two, nearest to μ_* provide the sidebands order best complying with the frequency matching. To find μ_*, we introduce a new parameter

$$\varepsilon_{\pm\mu} = \omega_{0\mathrm{f}} + \omega_{\pm\mu\mathrm{f}} - \omega_{\pm\mu\mathrm{s}} \tag{27}$$

[see Eq. (24)], so that

$$\Delta_{\pm\mu} = \varepsilon_{\pm\mu} - \delta. \tag{28}$$

We note that $\varepsilon_{\pm\mu}$ depend only on the resonator geometry and refractive index [see Eq. (10)]. Using Eq. (5), we express $\varepsilon_{\pm\mu}$ as

$$\varepsilon_{\pm\mu} = \varepsilon_0 \pm \mu(D_{1\mathrm{f}} - D_{1\mathrm{s}}) + \tfrac{1}{2}\mu^2(D_{2\mathrm{f}} - D_{2\mathrm{s}}). \tag{29}$$

Relative smallness of the dispersion, i.e., of the $\mu^2 D_{2\zeta}$ and δ terms, provides an excellent approximation for μ_*:

$$\mu_* \approx \frac{|\varepsilon_0|}{|D_{1\mathrm{f}} - D_{1\mathrm{s}}|}. \tag{30}$$

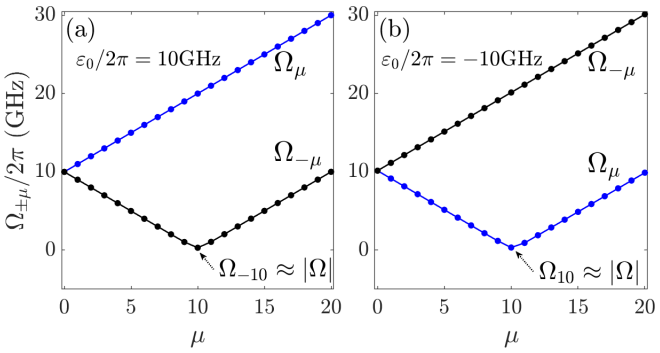

FIG. 5. Ω_μ and $\Omega_{-\mu}$ Rabi frequencies vs μ. (a) $\varepsilon_0/2\pi = 10.5$ GHz, and (b) $\varepsilon_0/2\pi = -10.5$ GHz, $\delta = 14\kappa_\mathrm{f}$, $|\Omega| = 300\kappa_\mathrm{f}$. $\Delta_{-\mu} = \omega_p + \omega_{-\mu\mathrm{f}} - \omega_{-\mu\mathrm{s}}$ is nearly matched for $\mu = 10$ in (a), and $\Delta_\mu = \omega_p + \omega_{\mu\mathrm{f}} - \omega_{\mu\mathrm{s}}$ is in (b).

If $\varepsilon_0 > 0$, then μ_* solves $\Delta_{-\mu} = 0$ [see Fig. 4(a)], and if $\varepsilon_0 < 0$, then μ_* solves $\Delta_\mu = 0$. This point is further facilitated in Fig. 5, where we plot Ω_μ and $\Omega_{-\mu}$ vs μ for different signs of ε_0. For $\varepsilon_0 > 0$, $\Omega_{-\mu}$ has a minimum at $\mu = \mu_* \approx \widehat{\mu}$, $\Omega_{-\mu_*} = |\Omega|$, and for $\varepsilon_0 < 0$, Ω_μ is the one with the minimum. The simple approximations for $\Omega_{\pm\mu}$ are also inferred from Fig. 5. For $\varepsilon_0 > 0$, we have

$$\begin{aligned} &\Omega_\mu \approx \Delta_\mu \text{ for all } \mu,\ \Omega_{-\mu} \approx \Delta_{-\mu} \text{ for } \mu < \widehat{\mu}, \\ &\Omega_{-\widehat{\mu}} \approx |\Omega| \text{ for } \mu = \widehat{\mu},\ \Omega_{-\mu} \approx -\Delta_{-\mu} \text{ for } \mu > \widehat{\mu}. \end{aligned} \tag{31}$$

The same approximations for $\varepsilon_0 < 0$ require the $\Omega_{\pm\mu} \to \Omega_{\mp\mu}$ swap in every part of Eq. (31) [see Fig. 5(b)].

VI. DRESSED STATES

Equation (15) has an obvious and important class of solutions with time-independent sideband powers—dressed (eigen) states. The Rabi oscillations stem from a superposition of the dressed states. Dressing the states, i.e., working with the superpositions between $\widetilde{\psi}_{\mu\mathrm{f}}$ and $\widetilde{\psi}_{\mu\mathrm{s}}$, rather than with the modes of the linear resonator, allows us to develop a theory embracing the cases with the arbitrary (small, large, or near 1) ratios of the $|\widetilde{\psi}_{\mu\mathrm{s}}|^2$ and $|\widetilde{\psi}_{\mu\mathrm{f}}|^2$ powers [23].

After the rescaling, $\widetilde{\psi}_{\pm\mu\mathrm{f}} = e^{\pm i\phi_\mathrm{f}}\tilde{a}_{\pm\mu\mathrm{f}}/\sqrt{2}$, $\widetilde{\psi}_{\pm\mu\mathrm{s}} = e^{\pm i\phi_\mathrm{s}}\tilde{a}_{\pm\mu\mathrm{s}}/\sqrt{\gamma_{2\mathrm{f}}/\gamma_{2\mathrm{s}}}$, $\phi_\zeta = \arg\psi_{0\zeta}$, Eqs. (12) become

$$i\partial_t|\tilde{a}_\mu\rangle = (\widehat{H}_\mu + \widehat{V})|\tilde{a}_\mu\rangle. \tag{32}$$

Here $|\tilde{a}_\mu\rangle = (\tilde{a}_{\mu\mathrm{f}}, \tilde{a}_{\mu\mathrm{s}}, \tilde{a}_{-\mu\mathrm{f}}, \tilde{a}_{-\mu\mathrm{s}})^T$ is the state vector,

$$\widehat{H}_\mu = \begin{bmatrix} \Delta_{\mu\mathrm{f}} & -\frac{1}{2}|\Omega|e^{-i\phi} & 0 & 0 \\ -\frac{1}{2}|\Omega|e^{i\phi} & \Delta_{\mu\mathrm{s}} & 0 & 0 \\ 0 & 0 & -\Delta_{-\mu\mathrm{f}} & \frac{1}{2}|\Omega|e^{i\phi} \\ 0 & 0 & \frac{1}{2}|\Omega|e^{-i\phi} & -\Delta_{-\mu\mathrm{s}} \end{bmatrix}, \tag{33}$$

$\phi = 2\phi_\mathrm{f} - \phi_\mathrm{s}$, and

$$\widehat{V} = \begin{bmatrix} -i\frac{1}{2}\kappa_\mathrm{f} & 0 & -\frac{|\Omega|^2 e^{-i\phi}}{|\Omega_\mathrm{s}|} & 0 \\ 0 & -i\frac{1}{2}\kappa_\mathrm{s} & 0 & 0 \\ \frac{|\Omega|^2 e^{i\phi}}{|\Omega_\mathrm{s}|} & 0 & -i\frac{1}{2}\kappa_\mathrm{f} & 0 \\ 0 & 0 & 0 & -i\frac{1}{2}\kappa_\mathrm{s} \end{bmatrix}. \tag{34}$$

Setting

$$\begin{aligned} |\tilde{a}(t)\rangle &= |a_\mu\rangle \exp\{t\lambda_\mu - it\beta_\mu\}, \\ \lambda_\mu &\in \mathbb{R},\ \beta_\mu \in \mathbb{R}, \end{aligned} \tag{35}$$

we find

$$(\beta_\mu + i\lambda_\mu)|a_\mu\rangle = (\widehat{H}_\mu + \widehat{V})|a_\mu\rangle, \tag{36}$$

where β_μ is the frequency shift, and λ_μ is the sideband growth rate, such that λ_μ transiting from negative to positive signals instability of the cw state relative to the excitation of the $\pm\mu$ pair.

In the SC regime [see Eq. (23)], $\widehat{V}$ is a perturbation to $\widehat{H}_\mu$, and therefore, before incorporating $\widehat{V}$, we look into the details of the dressed states:

$$\widehat{H}_\mu|b_\mu^{(j)}\rangle = \beta_\mu^{(j)}|b_\mu^{(j)}\rangle,\ j = 1, 2, 3, 4. \tag{37}$$

The eigenfrequencies, $\beta_\mu^{(j)}$, and state vectors, $|b_\mu^{(j)}\rangle$, of the four branches of the dressed spectrum are [23]

$$\begin{aligned} \beta_\mu^{(1)} &= \tfrac{1}{2}(\Delta_{\mu\mathrm{f}} + \Delta_{\mu\mathrm{s}}) + \tfrac{1}{2}\Omega_\mu, \\ |b_\mu^{(1)}\rangle &= |\Omega|e^{-i\phi}|1\rangle + (\Delta_\mu - \Omega_\mu)|2\rangle; \\ \beta_\mu^{(2)} &= \tfrac{1}{2}(\Delta_{\mu\mathrm{f}} + \Delta_{\mu\mathrm{s}}) - \tfrac{1}{2}\Omega_\mu, \\ |b_\mu^{(2)}\rangle &= |\Omega|e^{-i\phi}|1\rangle + (\Delta_\mu + \Omega_\mu)|2\rangle; \\ \beta_\mu^{(3)} &= -\tfrac{1}{2}(\Delta_{-\mu\mathrm{f}} + \Delta_{-\mu\mathrm{s}}) - \tfrac{1}{2}\Omega_{-\mu}, \\ |b_\mu^{(3)}\rangle &= |\Omega|e^{i\phi}|3\rangle + (\Delta_{-\mu} - \Omega_{-\mu})|4\rangle; \\ \beta_\mu^{(4)} &= -\tfrac{1}{2}(\Delta_{-\mu\mathrm{f}} + \Delta_{-\mu\mathrm{s}}) + \tfrac{1}{2}\Omega_{-\mu}, \\ |b_\mu^{(4)}\rangle &= |\Omega|e^{i\phi}|3\rangle + (\Delta_{-\mu} + \Omega_{-\mu})|4\rangle. \end{aligned} \tag{38}$$

The branches (1) and (2) describe the Rabi induced coupling between the $+\mu$ sidebands in the fundamental and second harmonic, and (3) and (4) do the same for the $-\mu$ sidebands. The corresponding dressed frequencies are

$$\begin{aligned} \widetilde{\omega}_{\mu\mathrm{f}}^{(1),(2)} &= \omega_p + \mu D_1 + \beta_\mu^{(1),(2)}, \\ \widetilde{\omega}_{\mu\mathrm{f}}^{(3),(4)} &= \omega_p - \mu D_1 - \beta_\mu^{(3),(4)}, \\ \widetilde{\omega}_{\mu\mathrm{s}}^{(1),(2)} &= 2\omega_p + \mu D_1 + \beta_\mu^{(1),(2)}, \\ \widetilde{\omega}_{\mu\mathrm{s}}^{(3),(4)} &= 2\omega_p - \mu D_1 - \beta_\mu^{(3),(4)}. \end{aligned} \tag{39}$$

Taking the explicit expressions for Δ_μ and $(\Delta_{\mu\mathrm{f}} + \Delta_{\mu\mathrm{s}})/2$ inside $\beta_\mu^{(j)}$ one would find that $\widetilde{\omega}_{\mu\zeta}^{(j)}$ are the reference frame, i.e., D_1, independent.

Power distribution between the fundamental and second-harmonic sidebands within a given branch and for a given μ is determined by the dressing parameters, $\Delta_{\pm\mu}^2/|\Omega|^2$. If the Rabi detuning is relatively large, i.e., a particular mode is far from being sum-frequency matched [see the points away from the zero line in Fig. 4(a)], then the corresponding dressed state, $|b_\mu^{(j)}\rangle$, tends towards an eigenstate of the bare, i.e., $\Omega = 0$, resonator. The bare states are

$$\begin{aligned} |1\rangle &= (1, 0, 0, 0)^T, & e^{i(M+\mu)\vartheta - it\omega_{\mu\mathrm{f}}}, \\ |2\rangle &= (0, 1, 0, 0)^T, & e^{i(2M+\mu)\vartheta - it\omega_{\mu\mathrm{s}}}, \\ |3\rangle &= (0, 0, 1, 0)^T, & e^{i(M-\mu)\vartheta - it\omega_{-\mu\mathrm{f}}}, \\ |4\rangle &= (0, 0, 0, 1)^T, & e^{i(2M-\mu)\vartheta - it\omega_{-\mu\mathrm{s}}}, \end{aligned} \tag{40}$$

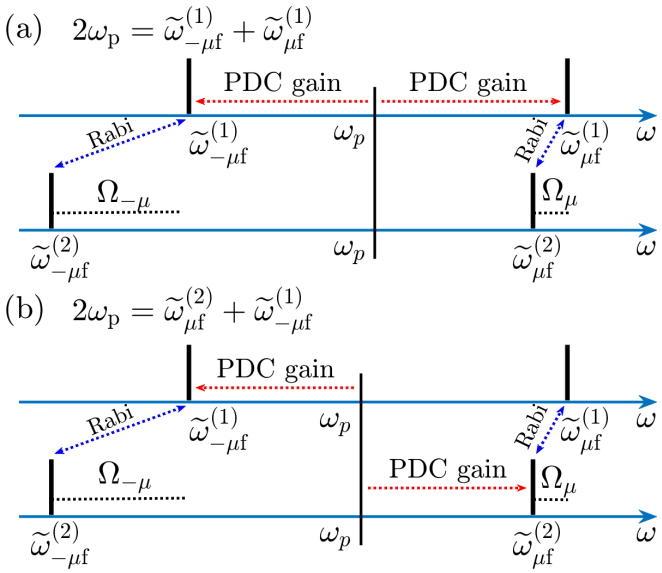

FIG. 6. Diagram illustrating the dressed spectra. (a) Pump frequency tuned to satisfy the intrabranch PDC condition, $\hbar 2\omega_p = \hbar\widetilde{\omega}^{(1)}_{\mu f} + \hbar\widetilde{\omega}^{(1)}_{-\mu f}$. (b) How the cross-branch PDC condition is satisfied, $\hbar 2\omega_p = \hbar\widetilde{\omega}^{(2)}_{\mu f} + \hbar\widetilde{\omega}^{(1)}_{-\mu f}$. The red and blue arrows show how the PDC gain and Rabi flops redistribute power within the spectrum. The black dotted lines show the Rabi frequencies, Ω_μ and $\Omega_{-\mu}$, and highlight their inequality.

where, for the sake of clarity, we explicitly associated each of the state vectors to the corresponding resonator mode.

The maximal dressing condition, $\Delta_{\pm\mu} = 0$, involves frequencies of the bare resonator, while the matching points are replaced by the avoided crossings in the dressed resonator [see Fig. 4(b)]. The avoided crossing between $\widetilde{\omega}^{(1)}_{\pm\mu\zeta}$ and $\widetilde{\omega}^{(2)}_{\pm\mu\zeta}$ exists for every μ; however, most of them do not come to the practical, tens of MHz, proximity of $\delta = 0$, apart from the ones nearest to $\pm\mu_*$.

Noting the symmetries

$$\begin{aligned} \beta^{(3)}_{\mu} &= -\beta^{(1)}_{-\mu}, \quad \text{i.e.,} \quad \widetilde{\omega}^{(1)}_{-\mu\zeta} = \widetilde{\omega}^{(3)}_{\mu\zeta}, \\ \beta^{(4)}_{\mu} &= -\beta^{(2)}_{-\mu}, \quad \text{i.e.,} \quad \widetilde{\omega}^{(2)}_{-\mu\zeta} = \widetilde{\omega}^{(4)}_{\mu\zeta}, \end{aligned} \tag{41}$$

we conclude that there are two ways to proceed from this point. First, the problem could be formulated using the four dressed frequencies, e.g., $\widetilde{\omega}^{(1)}_{\mu f}$, $\widetilde{\omega}^{(2)}_{\mu f}$, $\widetilde{\omega}^{(3)}_{\mu f}$, $\widetilde{\omega}^{(4)}_{\mu f}$ [23]. Second, one could switch to using the two-branch formulation and deal with $\widetilde{\omega}^{(1)}_{\mu f}$, $\widetilde{\omega}^{(1)}_{-\mu f}$, $\widetilde{\omega}^{(2)}_{\mu f}$, $\widetilde{\omega}^{(2)}_{-\mu f}$. The latter approach is slightly more intuitive and we choose to follow it here. In either case, the four frequencies and eigenstates have to be traced. The $\widetilde{\omega}^{(1)}_{\pm\mu f}$ and $\widetilde{\omega}^{(2)}_{\pm\mu f}$ frequencies in the dressed spectrum are illustrated in Fig. 6. The $\widetilde{\omega}^{(1)}_{\pm\mu s}$ and $\widetilde{\omega}^{(2)}_{\pm\mu s}$ spectra characterize the same dressed states as $\widetilde{\omega}^{(1)}_{\pm\mu f}$ and $\widetilde{\omega}^{(2)}_{\pm\mu f}$. If the former are plotted then they would make the same spectrum as in Fig. 6 apart from being centered at $2\omega_p$ [see Eq. (39)].

VII. DRESSED SPECTRUM AND ENERGY CONSERVATION IN PARAMETRIC DOWN CONVERSION

In any parametric system, the parametric resonance is achieved for, usually, a sequence of the resonance values of the drive frequency [43]. In optical resonators in general, and in the dressed $\chi^{(2)}$ system, in particular, this is done by tuning ω_p to the midpoint between the desired sidebands, e.g., $\widetilde{\omega}^{(1)}_{\mu f}$ and $\widetilde{\omega}^{(1)}_{-\mu f}$. One peculiar feature of our case is that the dressed resonances depend on the pump power and frequency. Another is that for the two pairs of frequencies, $\widetilde{\omega}^{(1)}_{\pm\mu f}$ and $\widetilde{\omega}^{(2)}_{\pm\mu f}$, there could be four different midpoints for the same μ, and hence four conditions providing the maximum of the parametric gain [23,44]:

$$2\hbar\omega_p = \hbar\widetilde{\omega}^{(1)}_{\mu f} + \hbar\widetilde{\omega}^{(1)}_{-\mu f}, \quad \left(\beta^{(1)}_{\mu} = -\beta^{(1)}_{-\mu}\right), \tag{42a}$$

$$2\hbar\omega_p = \hbar\widetilde{\omega}^{(2)}_{\mu f} + \hbar\widetilde{\omega}^{(2)}_{-\mu f}, \quad \left(\beta^{(2)}_{\mu} = -\beta^{(2)}_{-\mu}\right), \tag{42b}$$

$$2\hbar\omega_p = \hbar\widetilde{\omega}^{(1)}_{\mu f} + \hbar\widetilde{\omega}^{(2)}_{-\mu f}, \quad \left(\beta^{(1)}_{\mu} = -\beta^{(2)}_{-\mu}\right), \tag{42c}$$

$$2\hbar\omega_p = \hbar\widetilde{\omega}^{(2)}_{\mu f} + \hbar\widetilde{\omega}^{(1)}_{-\mu f}, \quad \left(\beta^{(2)}_{\mu} = -\beta^{(1)}_{-\mu}\right). \tag{42d}$$

The auxiliary frequency $\widetilde{\omega}_\mu = \omega_p + \mu D_{1f} + \frac{1}{2}(\Delta_{\mu f} + \Delta_{\mu s})$ makes the role of the Rabi splitting in the above more transparent:

$$2\hbar\omega_p = \hbar\left(\widetilde{\omega}_\mu + \tfrac{1}{2}\Omega_\mu\right) + \hbar\left(\widetilde{\omega}_{-\mu} + \tfrac{1}{2}\Omega_{-\mu}\right), \tag{43a}$$

$$2\hbar\omega_p = \hbar\left(\widetilde{\omega}_\mu - \tfrac{1}{2}\Omega_\mu\right) + \hbar\left(\widetilde{\omega}_{-\mu} - \tfrac{1}{2}\Omega_{-\mu}\right), \tag{43b}$$

$$2\hbar\omega_p = \hbar\left(\widetilde{\omega}_\mu + \tfrac{1}{2}\Omega_\mu\right) + \hbar\left(\widetilde{\omega}_{-\mu} - \tfrac{1}{2}\Omega_{-\mu}\right), \tag{43c}$$

$$2\hbar\omega_p = \hbar\left(\widetilde{\omega}_\mu - \tfrac{1}{2}\Omega_\mu\right) + \hbar\left(\widetilde{\omega}_{-\mu} + \tfrac{1}{2}\Omega_{-\mu}\right). \tag{43d}$$

The first pair of conditions, Eqs. (42a) and (42b), corresponds to the intrabranch PDC, which is satisfied by tuning the pump frequency to the midpoint between $\widetilde{\omega}^{(j)}_{\mu f}$ and $\widetilde{\omega}^{(j)}_{-\mu f}$. The second pair, Eqs. (42c) and (42d), are the cross-branch PDC conditions. They are satisfied by ω_p being tuned to the midpoint between the μ and $-\mu$ sidebands from the two different branches of the dressed spectrum.

Figure 6 illustrates achieving frequency matching for the intra- and cross-branch cases, and also shows how the effective Rabi frequencies, $\Omega_{\pm\mu}$, come into play. Ω_μ and $\Omega_{-\mu}$ are generally very different, and coincide only for $\mu = 0$ (see Fig. 5).

To gain further important insights into the PDC conditions in Eq. (42), we rearrange them as

$$\varepsilon^{(j_1,j_2)}_{\mu} = \widetilde{\omega}^{(j_1)}_{\mu f} + \widetilde{\omega}^{(j_2)}_{-\mu f} - 2\omega_p \tag{44}$$

and plot $\varepsilon^{(j_1,j_2)}_{\mu}$ vs μ (see Fig. 7). The sideband numbers grouped around the zero lines correspond to the MHz level mismatches that are more easily compensated by the nonlinear effects providing $\varepsilon^{(j_1,j_2)}_{\mu} = 0$. The sidebands with $\varepsilon^{(j_1,j_2)}_{\mu}$ detuned away from zero by the GHz offsets [see the black dots in Figs. 7(a) and 7(b)] are cut off from the groups of the PDC capable mode numbers. The cutoff is happening for μ's around μ_*, corresponding to the sum-frequency matching [see Eq. (30)].

Figure 7(a) shows that the intrabranch condition in Eq. (42a) can be satisfied for $0 \leqslant \mu \lesssim \mu_*$, while ε_0 is set to be positive. The second intrabranch condition, Eq. (42b) [see Fig. 7(c)], is shifted away from zero by $\approx 2\varepsilon_0$, and will be swapped with the first one for $\varepsilon_0 \to -\varepsilon_0$. Figures 7(b) and

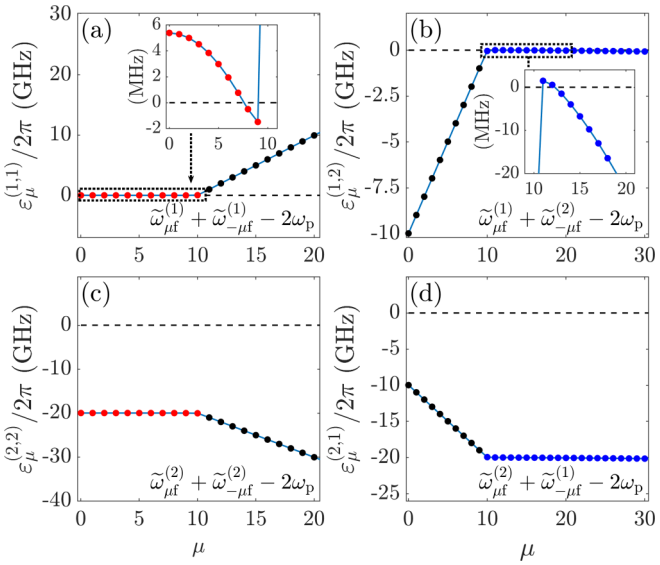

FIG. 7. Frequency matching parameters $\varepsilon_\mu^{(j_1 j_2)} = \widetilde{\omega}_{\mu_1 f}^{(j_1)} + \widetilde{\omega}_{\mu_2 f}^{(j_2)} - 2\omega_p$ for the four types of the parametric down conversion (PDC) conditions. The sideband numbers grouped around the dashed horizontal lines, $\varepsilon_\mu^{(j_1 j_2)} = 0$, correspond to the MHz mismatches that can be compensated by the nonlinear effects and lead to the exact PDC frequency matching (see insets). (a, b) $\delta = 2.55\kappa_f$, $|\Omega|/2\pi = 76$ MHz. (c, d) $\delta = 8.1\kappa_f$, $|\Omega|/2\pi = 105$ MHz, and $\varepsilon_0/2\pi = 10$ GHz. $\mu \approx 10$ (see the corner points) corresponds to the sum-frequency matching, $\Delta_{-\mu} \approx 0$.

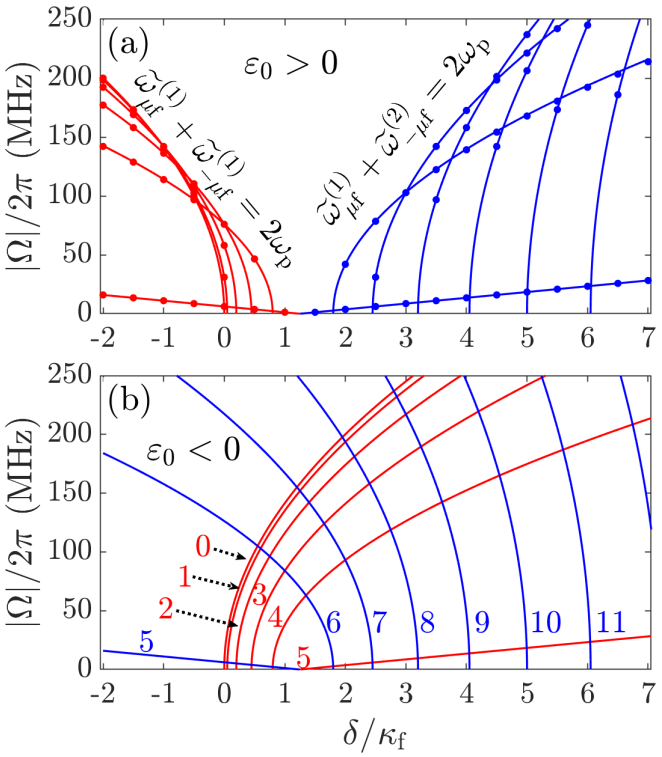

FIG. 8. Lines corresponding to the exact PDC frequency matching conditions in the parameter space of the pump detuning, δ, and of the Rabi frequency, $|\Omega|$, characterizing the intraresonator cw power (see Fig. 2). The red lines (numbered 0 to 5) correspond to the intrabranch PDCs, which are $\hbar\widetilde{\omega}_{\mu f}^{(1)} + \hbar\widetilde{\omega}_{-\mu f}^{(1)} = \hbar 2\omega_p$ in (a) where $\varepsilon_0/2\pi = 5$ GHz, and $\hbar\widetilde{\omega}_{\mu f}^{(2)} + \hbar\widetilde{\omega}_{-\mu f}^{(2)} = \hbar 2\omega_p$ in (b) where $\varepsilon_0/2\pi = -5$ GHz, $0 \leqslant \mu \leqslant 5$. The blue lines (numbered 5 to 11) correspond to the cross-branch PDCs, which are $\hbar\widetilde{\omega}_{\mu f}^{(1)} + \hbar\widetilde{\omega}_{-\mu f}^{(2)} = \hbar 2\omega_p$ in (a), and $\hbar\widetilde{\omega}_{\mu f}^{(2)} + \hbar\widetilde{\omega}_{-\mu f}^{(1)} = \hbar 2\omega_p$ in (b), $\mu \geqslant 5$. The lines in (a) and (b) use Eq. (45), while the dots in (a) are derived from the approximate Eq. (46) for $\mu \neq 5$ and Eq. (E5) for $\mu = 5$.

7(d) show the cross-branch PDC conditions, with one of them being satisfied for $\mu \gtrsim \mu_*$.

The challenge with resolving Eq. (42) analytically for either Ω or δ is in the occurrences of them under the square-root sign in the equation for Ω_μ (see Table II). However, the algebra is proceedable [23,44], and leads to finding that all four PDC conditions are resolved by $|\Omega| = |\Omega_{\rm pdc}|$, where

$$|\Omega_{\rm pdc}|^2 = 4(\Delta_{\mu f} + \Delta_{-\mu f})(\Delta_{\mu s} + \Delta_{-\mu s}) \times \frac{(\Delta_{\mu f} + \Delta_{-\mu s})(\Delta_{\mu s} + \Delta_{-\mu f})}{(\Delta_{\mu f} + \Delta_{-\mu f} + \Delta_{\mu s} + \Delta_{-\mu s})^2}. \quad (45)$$

Plots of $|\Omega_{\rm pdc}|$ vs δ for positive and negative ε_0, and their associations with the PDC conditions, are shown in Fig. 8. These plots in Fig. 8 could be compared with the temperature tuning diagrams of the parametric oscillators (see, e.g., Refs. [33–35]), but in our case, the temperature is assumed fixed, while the tuning parameters are the pump power expressed via $|\Omega|$, and the pump frequency. The range of $|\Omega|$s considered by us provides relatively small intraresonator powers, on the order of mW to <1W (cf. the left and right axes in Fig. 9).

If $|\varepsilon_0|$ dominates over all δ's, and μ_* falls between the two nearest integers, i.e., the exact sum-frequency matching point has been missed, then Eq. (45) simplifies to

$$|\Omega_{\rm pdc}|^2 \approx -4\varepsilon_0(\delta - \delta_{\mu f})\left[1 - \frac{\mu^2}{\mu_*^2}\right], \delta_{\mu f} = -\frac{1}{2}D_{2f}\mu^2 \quad (46)$$

(see Appendix E for details).

Equation (46) reveals what has been described above based on the numerical plots. First, one can see that the resonances converge to points $\delta = \delta_{\mu f}$ for $\Omega \to 0$, which corresponds to the zero of the first bracket in the numerator of Eq. (45). Second, the direction of the nonlinearity induced tilts of the resonances depends on the sign of ε_0 and the value of μ (see Fig. 8). If $\varepsilon_0 < 0$, then the tilt is towards $\delta > \delta_{\mu f}$ for $0 \leqslant \mu < \mu_*$, and towards $\delta < \delta_{\mu f}$ for $\mu > \mu_*$. $\varepsilon_0 > 0$ changes the tilt direction for the two groups of modes.

Figure 8 also shows a good agreement between the exact and approximate $|\Omega_{\rm pdc}|^2$ vs δ dependencies. Analytical approximation for $|\Omega_{\rm pdc}|$ in the case when the sum-frequency process is either nearly or exactly matched, i.e., $\mu = \widehat{\mu} \approx \mu_*$, is considered in Appendix E.

To summarize, the intrabranch PDC conditions are satisfied for a compact group of sideband numbers,

$$0 \leqslant \mu \leqslant \mu_*, \text{ i.e., for} \left[1 - \frac{\mu^2}{\mu_*^2}\right] \geqslant 0, \quad (47)$$

while the cross-branch ones are engaged for the unbound set of sidebands,

$$\mu \geqslant \mu_*, \text{ i.e., for} \left[1 - \frac{\mu^2}{\mu_*^2}\right] \leqslant 0. \quad (48)$$

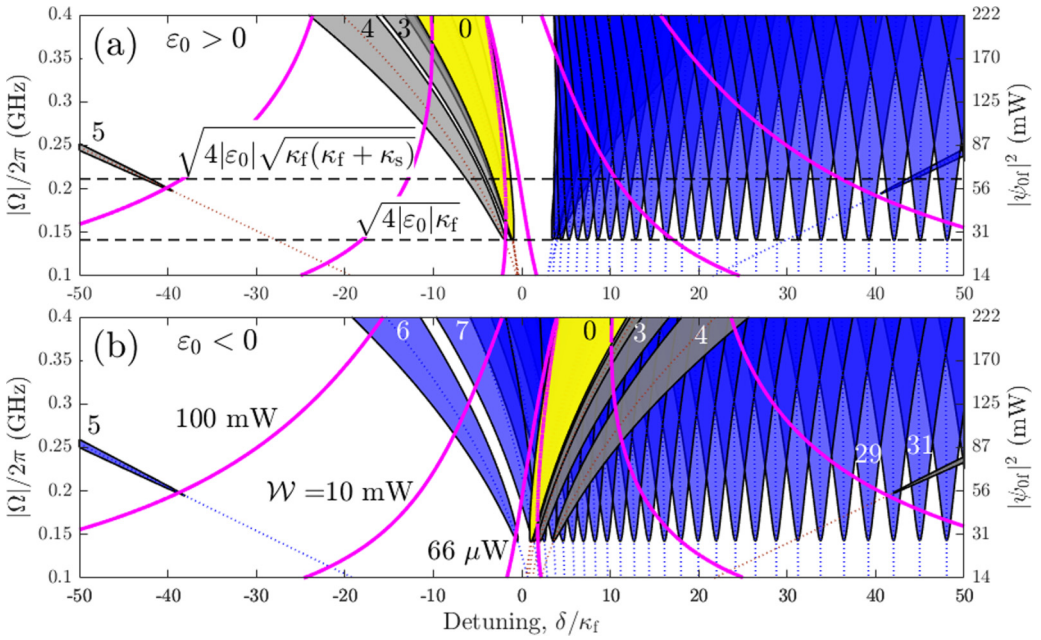

FIG. 9. Parametric down conversion (PDC) instability tongues mapped onto the parameter space spanned by the laser detuning, δ, and the Rabi frequency, $|\Omega|$ (see the left axis), or, and equivalently, by the intraresonator cw power, $|\psi_{0f}|^2$ (see the right axis). (a) $\varepsilon_0/2\pi = 5$ GHz. (b) $\varepsilon_0/2\pi = -5$ GHz. The gray shaded tongues correspond to the intrabranch PDC conditions marked by the red lines in Fig. 8, and the blue tongues correspond to the cross-branch PDCs. Some of the tongues are marked with the respective μ's (see Fig. 8 for the complete illustration of the μ ordering). The magenta lines show $|\Omega| = |\psi_{0f}|\sqrt{8\gamma_f\gamma_s}$ vs δ achieved for the laser powers $\mathcal{W} = 66$ μW, 10 mW, and 100 mW.

Thus, the sum-frequency matched sideband, μ_* or $-\mu_*$, defines the transition between the two different PDC scenarios.

VIII. PDC INSTABILITY TONGUES

While the PDC frequency matching provides conditions for the maximal parametric gain, the latter still needs to overcome the dissipation in order to trigger the exponential growth of sidebands, i.e., to induce the cw instabilities. Regions of the PDC instabilities for every $\pm\mu$ pair of sidebands can be computed numerically by solving the eigenvalue problem in Eq. (36) and plotting the lines $\lambda_\mu = 0$ [23]. Every μ-specific instability area is represented by a tonguelike domain shaped around the respective $|\Omega_{pdc}|$ vs δ line (see Figs. 8 and 9).

The intrabranch instabilities, Eqs. (42a) and (42b), are colored in gray in Fig. 9, while the cross-branch ones, Eqs. (42c) and (42d), are shown in blue. The magenta lines show $|\Omega|$'s vs δ corresponding to the cw state achieved for three representative values of the laser power, $\mathcal{W} = 66$ μW, 10 mW, and 100 mW. The cw state is expressed via Ω as per Eq. (18), while Ω itself is a solution of

$$\Omega = \sqrt{\frac{\kappa_f\kappa_s}{2}}\sqrt{\frac{\mathcal{W}}{\mathcal{W}_*}}\frac{\kappa_f}{\Omega_f}\left[1-\frac{|\Omega|^2}{\Omega_f\Omega_s}\right]^{-1}, \tag{49}$$

where $\Omega_f = \delta - i\frac{1}{2}\kappa_f$, $\Omega_s = 8(2\delta - i\frac{1}{2}\kappa_s) - 8\varepsilon_0$, $\mathcal{W}$ is the laser power in watts, and $\mathcal{W}_*$ is its scaling [see Eq. (C5)]. Taking the modulus squared of Eq. (49) we find a real cubic equation for $|\Omega|^2$, that can have either one or three positive roots, with the latter case signaling the cw bistability (see Fig. 2, and further details in Appendix C).

Thus, a scan of the laser frequency, ω_p, would go along an individual power-defined path crossing the different PDC domains (see the magenta lines in Fig. 9). The yellow shading marks the $\mu = 0$ tongue embracing the middle branch of the bistability loop (see Fig. 2). For the Kerr resonators, similar tongue diagrams were recently reported in Refs. [45,46].

IX. PARAMETRIC THRESHOLDS

PDC thresholds, i.e., the minimal intraresonator powers triggering the exponential growth of the $\pm\mu$ sideband pairs, happen at the tips of the instability tongues (see Fig. 9). To find the threshold when the system is confined to the $|\mu|$-specific PDC lines (see Figs. 8 and 9), we apply the degenerate state perturbation theory to Eq. (36) by treating $\widehat{V}$ as a perturbation to $\widehat{H}_\mu$, which is valid in the SC regime. The generic condition for the parametric gain to overcome losses has been introduced in Ref. [23]:

$$V_\mu^{(j_1j_2)}\cdot V_\mu^{(j_2j_1)} = V_\mu^{(j_1j_1)}\cdot V_\mu^{(j_2j_2)}, \tag{50}$$

where $V_\mu^{(j_1j_2)} = \langle b_\mu^{(j_1)}|\widehat{V}|b_\mu^{(j_2)}\rangle$ are the matrix elements of $\widehat{V}$.

Opening up Eq. (50) for $(j_1, j_2) = (1, 3)$, $(j_1, j_2) = (2, 4)$, $(j_1, j_2) = (1, 4)$, and $(j_1, j_2) = (2, 3)$ yields four threshold conditions:

$$\left[\kappa_f+\kappa_s\frac{(\Delta_\mu-\Omega_\mu)^2}{|\Omega|^2}\right]\left[\kappa_f+\kappa_s\frac{(\Delta_{-\mu}-\Omega_{-\mu})^2}{|\Omega|^2}\right] = \frac{4|\Omega|^4}{|\Omega_s|^2}, \tag{51a}$$

$$\left[\kappa_f+\kappa_s\frac{(\Delta_\mu+\Omega_\mu)^2}{|\Omega|^2}\right]\left[\kappa_f+\kappa_s\frac{(\Delta_{-\mu}+\Omega_{-\mu})^2}{|\Omega|^2}\right] = \frac{4|\Omega|^4}{|\Omega_s|^2}, \tag{51b}$$

$$\left[\kappa_{\rm f}+\kappa_{\rm s}\frac{(\Delta_\mu-\Omega_\mu)^2}{|\Omega|^2}\right]\left[\kappa_{\rm f}+\kappa_{\rm s}\frac{(\Delta_{-\mu}+\Omega_{-\mu})^2}{|\Omega|^2}\right]=\frac{4|\Omega|^4}{|\Omega_{\rm s}|^2}, \tag{51c}$$

$$\left[\kappa_{\rm f}+\kappa_{\rm s}\frac{(\Delta_\mu+\Omega_\mu)^2}{|\Omega|^2}\right]\left[\kappa_{\rm f}+\kappa_{\rm s}\frac{(\Delta_{-\mu}-\Omega_{-\mu})^2}{|\Omega|^2}\right]=\frac{4|\Omega|^4}{|\Omega_{\rm s}|^2}. \tag{51d}$$

Equations (51) express the balance between the PDC gain (right) and the net loss (left). The second-harmonic losses, $\kappa_{\rm s}$, are weighted by the coefficients characterizing the power distribution between the components in the state vectors [see Eq. (38)]. The explicit threshold condition presented in Ref. [23] transforms to Eq. (51c) after making use of the identity $\frac{|\Omega|}{\Omega_\mu-\Delta_\mu}=\frac{\Omega_\mu+\Delta_\mu}{|\Omega|}$.

We now note that in the SC regime $|\Omega_{\rm s}|\approx 8|\varepsilon_0|$ [see Eq. (22)], and hence the right-hand sides in Eq. (51) are approximated with $|\Omega|^4/16|\varepsilon_0|^2$. To simplify the threshold conditions we make use of the approximations in Eq. (31) related to the case of $\varepsilon_0>0$ and $\Omega_{-\widehat{\mu}}\approx|\Omega|$ [see Fig. 5(a)]. Then, for $\mu<\widehat{\mu}$ both coefficients after $\kappa_{\rm s}$ in Eq. (51a) are small and can be omitted in the leading order, so that the threshold is determined by $\kappa_{\rm f}$ only and is well approximated by

$$\left|\Omega_{\rm th}^{(\mu)}\right|^2\approx 4|\varepsilon_0|\kappa_{\rm f},\ \mu\neq\widehat{\mu} \tag{52}$$

[see the gray tongues in Fig. 9(a)]. For $\mu>\widehat{\mu}$ the left-hand side of Eq. (51a) becomes $\approx 4\kappa_{\rm f}\kappa_s|\Delta_{-\mu}|^2/|\Omega|^2$, which creates prohibitively large power thresholds (see the cutoff transitions in Fig. 7).

For $\mu=\widehat{\mu}$, the threshold is approximated by

$$\left|\Omega_{\rm th}^{(\widehat{\mu})}\right|^2\approx 4|\varepsilon_0|\sqrt{\kappa_{\rm f}(\kappa_{\rm f}+\kappa_{\rm s})}. \tag{53}$$

$\kappa_{\rm s}$ is now also impacting the threshold, but still in a way that is not equally important with $\kappa_{\rm f}$. This is because the powers of the fundamental and second harmonic are balanced only for $\widetilde{\omega}^{(1)}_{-\widehat{\mu}\rm f}$ and $\widetilde{\omega}^{(1)}_{-\widehat{\mu}\rm s}$, but not for $\widetilde{\omega}^{(1)}_{\widehat{\mu}\rm f}$ and $\widetilde{\omega}^{(1)}_{\widehat{\mu}\rm s}$ sidebands. In the latter pair, the sum-frequency condition is mismatched, and hence the second-harmonic sideband is still very weak and can be disregarded, i.e., $\Delta_{\widehat{\mu}}\approx\Omega_{\widehat{\mu}}$ in Eq. (51a), while the approximations that work in the minus bracket are $\Delta_{-\widehat{\mu}}\approx 0$ and $\Omega_{-\widehat{\mu}}\approx|\Omega|$.

The first cross-branch condition, Eq. (51c), has a practical threshold at $\mu=\widehat{\mu}$ as in Eq. (53), and for $\mu>\widehat{\mu}$ as in Eq. (52) [see the blue tongues in Fig. 9(a)]. The second intrabranch, Eq. (51b), and second cross-branch, Eq. (51d), conditions do not create practical thresholds for $\varepsilon_0>0$, and play their roles for $\varepsilon_0<0$ [see Figs. 8(b) and 9(b)].

The analytical estimates for the detuning values where the μ-specific instabilities first happen, i.e., locations of the tips of the instability tongues, and the respective laser powers are derived in Appendix F.

X. ENVELOPE AND COUPLED-MODE EQUATIONS FOR MODE-LOCKED COMBS

We anticipate that the frequency comb solutions bifurcate from the μ-specific boundaries of the instability tongues in Fig. 9 (see Ref. [45]). Since we are going to continue to number the sidebands within the combs with μ, we use below the letter $\nu=1,2,3,\dots$ to mark the comb states with the sideband spacing given by ν. We seek the mode-locked combs as the solutions of the equation that couple all the modes through all the allowed nonlinear coupling terms [see Eq. (A1) in Appendix A].

The mode-locked combs are assumed to have the period $2\pi/\nu$, i.e., $\psi_\zeta(t,\vartheta)=\psi_\zeta(t,\vartheta+2\pi/\nu)$, and, therefore, we use the substitution

$$\psi_\zeta(t,\vartheta)=\Psi_{\nu\zeta}(\theta_\nu),\theta_\nu=\nu(\vartheta-D_{1\nu}t). \tag{54}$$

Here θ_ν is a new auxiliary coordinate, such that the period 2π in θ_ν corresponds to the period $2\pi/\nu$ in θ, $\Psi_{\nu\zeta}(\theta_\nu)=\Psi_{\nu\zeta}(\theta_\nu+2\pi)$. $D_{1\nu}$ is an unknown comb repetition rate generally different from either $D_{1\rm f}$ or $D_{1\rm s}$. If the reference frame is chosen to rotate with $D_{1\rm f}$, then $D_{1\nu}\neq D_{1\rm f}$ would imply the relative rotation with the $D_{1\nu}-D_{1\rm f}$ rate, leading to the tilted spatiotemporal profiles like in the bottom row in Fig. 10.

The selection mechanisms of the velocity of the dissipative $\chi^{(2)}$ solitons, equivalent to the selection of $D_{1\nu}$, have been discussed before the microresonator combs came into existence [27]. This selection is a generic aspect also encountered in, e.g., the equations with the higher-order dispersion terms [47], and in the cases showing the spontaneous symmetry-breaking effects [45].

Substituting Eq. (54) into Eq. (A1) we find

$$\begin{aligned}
&\delta\Psi_{\nu\rm f}-i\nu(D_{1\rm f}-D_{1\nu})\frac{d\Psi_{\nu\rm f}}{d\theta_\nu}-\frac{\nu^2D_{2\rm f}}{2}\frac{d^2\Psi_{\nu\rm f}}{d\theta_\nu^2}\\
&-\gamma_{\rm f}\Psi_{\nu\rm s}\Psi^*_{\nu\rm f}-\frac{i\kappa_{\rm f}}{2}(\Psi_{\nu\rm f}-\mathcal{H})=0,\\
&(2\delta-\varepsilon_0)\Psi_{\nu\rm s}-i\nu(D_{1\rm s}-D_{1\nu})\frac{d\Psi_{\nu\rm s}}{d\theta_\nu}-\frac{\nu^2D_{2\rm s}}{2}\frac{d^2\Psi_{\nu\rm s}}{d\theta_\nu^2}\\
&-\gamma_{\rm s}\Psi^2_{\nu\rm f}-\frac{i\kappa_{\rm s}}{2}\Psi_{\nu\rm s}=0.
\end{aligned} \tag{55}$$

As one can see, the use of θ_ν as an argument has allowed us to conveniently sort the mode-locked combs by the spacing, ν, their sidebands make in the momentum space, since ν enters Eq. (55) explicitly. In fact, ν plays a role of the Bloch momentum which is now quantized, unlike the one that varies continuously in the theory of the unbound crystal lattices [48] and resonators [49].

For the frequency combs with the spatial period $2\pi/\nu$, the modes making nonzero contributions to the $\Psi_{\nu\zeta}$ have numbers $\mu=\nu m$, where $m=0,\pm1,\pm2,\pm3,\dots$ is another integer:

$$\Psi_{\nu\zeta}=\sum_{m=-\infty}^{\infty}\Psi_{m\nu\zeta}e^{im\theta_\nu}=\sum_{m=-\infty}^{\infty}\Psi_{m\nu\zeta}e^{im\nu(\vartheta-D_{1\nu}t)}. \tag{56}$$

Here $\Psi_{m\nu\zeta}$ are constants satisfying an algebraic system of equations [see Eq. (57)]. The repetition rate with which the $2\pi/\nu$ state is reproducing itself while rotating in the resonator is $\nu D_{1\nu}/2\pi$.

The coupling between the different $m\nu$ sidebands is provided by the sequence, i.e., cascade, of the sum-frequency

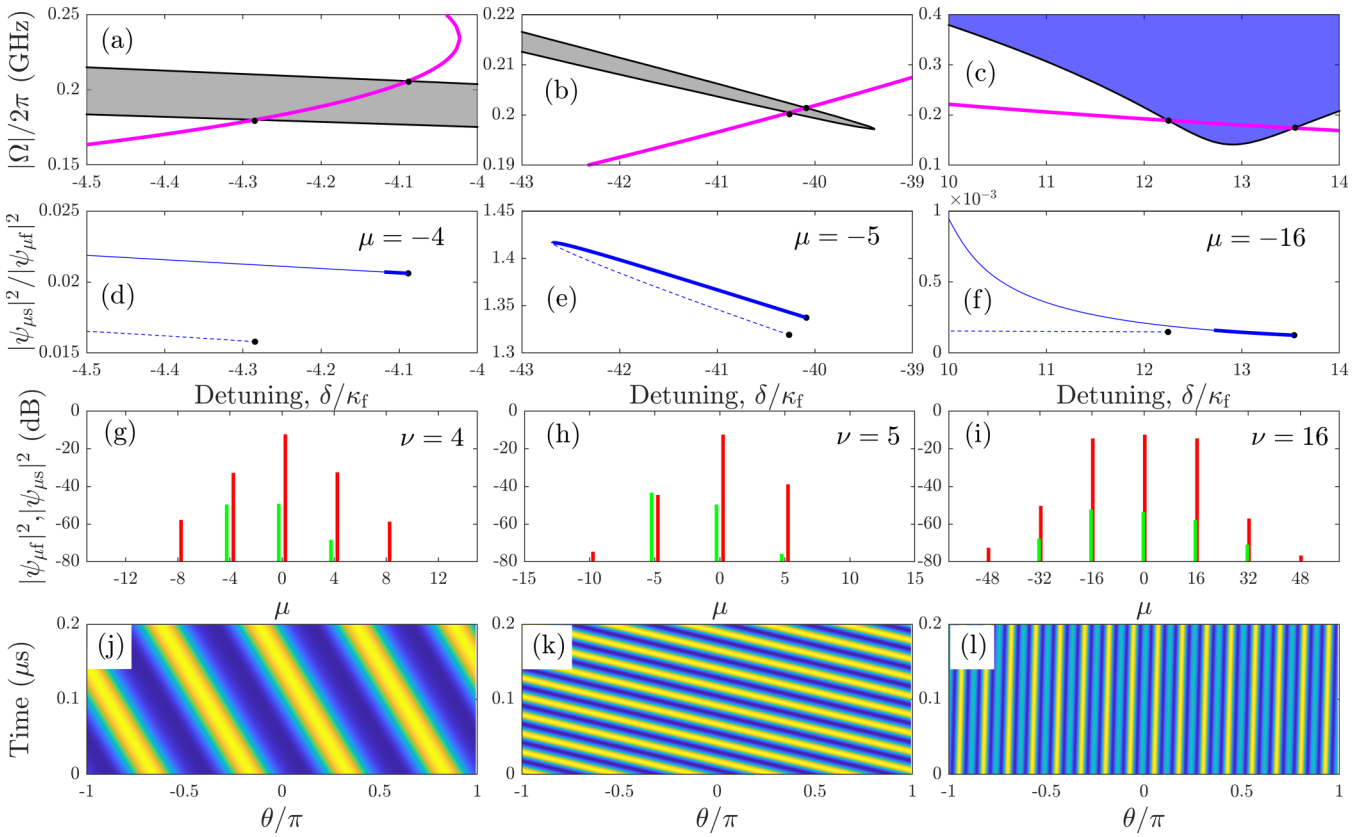

FIG. 10. Examples of the Turing-pattern frequency combs for $\varepsilon_0/2\pi = 5$ GHz. First and second columns show the combs emerging from the intrabranch PDC instability tongues [gray areas in (a) and (b)], and the third column shows the cross-branch PDC tongue [blue area in (c)] and the associated comb. Magenta lines in (a)–(c) show the cw states, $|\Omega| = |\psi_{0f}|\sqrt{8\gamma_f\gamma_s}$ vs δ. The respective laser powers (a) $\mathcal{W} = 0.664$ mW, (b) 103 mW, and (c) 10 mW. $|\Omega|/2\pi = 0.2$ GHz corresponds to the intraresonator power $|\psi_{0f}|^2 \simeq 55$ mW. (d–f) Ratio of the second harmonic and fundamental powers in the indicated sidebands. The $\mu = -5$ case corresponds to the sum-frequency matching leading to the best conversion efficiency. The thick full lines are stable solutions, and the thin lines (full and dashed) are unstable. (g–i) Self-explanatory spectra of the Turing patterns (red, fundamental; green, second harmonic). (j–l) Space-time profiles of the corresponding Turing patterns. The tilt relative to the vertical axis characterizes deviation of the pattern repetition rate from D_{1f}.

and difference-frequency events, which become evident on substituting Eq. (56) into Eq. (55):

$$\Delta_{m\nu f}\Psi_{m\nu f} - \frac{i\kappa_f}{2}(\Psi_{m\nu f} - \widehat{\delta}_{m,0}\mathcal{H}) - \gamma_f \sum_{m_1 m_2} \widehat{\delta}_{m,m_1-m_2}\Psi_{m_1\nu s}\Psi^*_{m_2\nu f} = 0, \tag{57a}$$

$$\Delta_{m\nu s}\Psi_{m\nu s} - \frac{i\kappa_s}{2}\Psi_{m\nu s} - \gamma_s \sum_{m_1 m_2} \widehat{\delta}_{m,m_1+m_2}\Psi_{m_1\nu f}\Psi_{m_2\nu f} = 0. \tag{57b}$$

The sideband detunings, $\Delta_{m\nu\zeta}$, are defined in Eq. (7), where $\mu = m\nu$. $\widehat{\delta}_{m,m_1\pm m_2} = 1$ for $m = m_1 \pm m_2$ and is zero otherwise. Hence, every term inside the nonlinear sums in Eqs. (57a) and (57b) corresponds to the momentum conservation laws,

$$\hbar(M + m\nu) = \hbar(2M + m_1\nu) - \hbar(M + m_2\nu), \tag{58a}$$

$$\hbar(2M + m\nu) = \hbar(M + m_1\nu) + \hbar(M + m_2\nu), \tag{58b}$$

describing the sum- and difference-frequency cascades. The left- and right-hand sides of Eq. (58) correspond to the linear and nonlinear terms in Eq. (57), respectively.

XI. TURING-PATTERN COMBS

The comb equations, Eqs. (55) and (57), have been solved by us with a Newton method allowing us to self-consistently find the sideband amplitudes, $\Psi_{m\nu\zeta}$, and the comb repetition rate, $D_{1\nu}$. Figure 10 shows how the comb branches with different periods, $2\pi/\nu$, emanate from the boundaries of the respective instability tongues.

The sparse combs, $\nu \gg 1$, described by a combination of few noticeable $\mu = \nu m$ sidebands have been observed and modeled in connection to several recent $\chi^{(2)}$-resonator experiments (see, e.g., Refs. [11–13,24]). In the context of the Kerr microresonators, the combs with the sparse spectra, as in Fig. 10, are often called the Turing-pattern frequency combs [45,50,51]. The Kerr microresonator instability tongues and their connection to the Turing patterns have been reported in Refs. [45,46]. The prior to the ring microresonator era results on the spatial pattern formation in the planar $\chi^{(2)}$ resonators can be found in, e.g., Refs. [52–58].

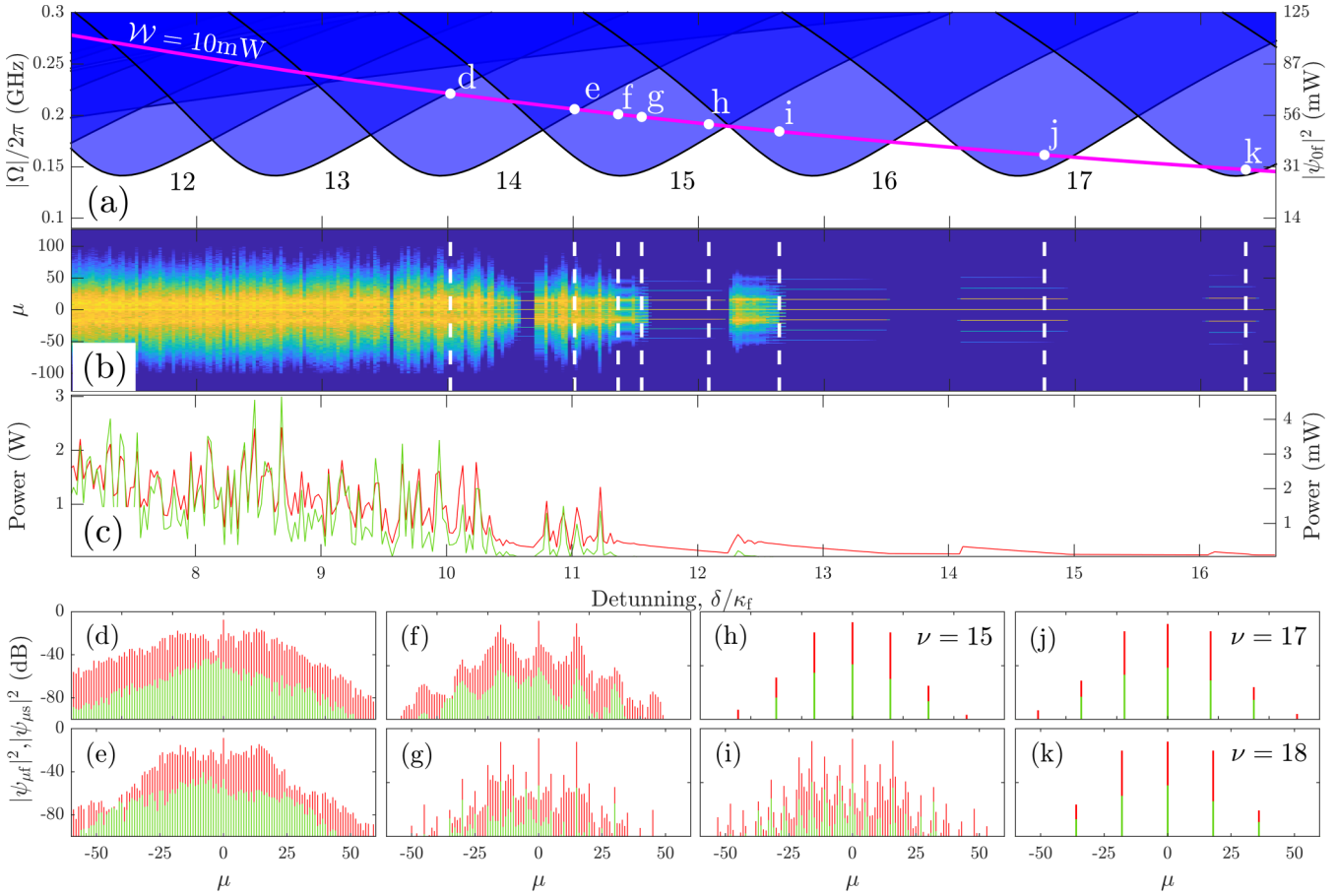

FIG. 11. (a) PDC instability tongues for $\mu = 12$–18, $\varepsilon_0/2\pi = 5$ GHz as in Fig. 9(a). The magenta line shows the cw state for the laser power $\mathcal{W} = 10$ mW. The left axis is the Rabi frequency, $|\Omega|$, and the right axis is the intraresonator cw power, $|\psi_{0f}|^2$. (b) The spectrum computed from the scan of the cw frequency along the magenta line in (a). (c) The integrated intraresonator powers corresponding to (b). The red line (left axis) is the fundamental, and the green line (right axis) is the second harmonic. Panels in the two bottom lines show the comb spectra computed at the detunings marked with the respective letters in (a), and with the dashed white lines in (b). In the two bottom rows, the shorter bars are plotted in green and the longer ones are plotted in red.

A typical bifurcation scenario that we found is that the two Turing-comb branches split from the two edges of the tongues and extend well beyond the tongues. The branch crossing into the tongue area can be stable (full lines in the second row in Fig. 10), while the one deviating outside the tongue (dashed lines) is always unstable. These two branches coalesce for some detuning value [see Fig. 10(e)]. The Turing combs emerging from the intrabranch PDC conditions for $\nu = 4, 5$ are shown in the first two columns in Fig. 10, and the $\nu = 16$ cross-branch case is shown in the third column.

The $\nu = 5$ tongue in Fig. 10(b) corresponds to the $\omega_p + \omega_{-5f} - \omega_{-5s} = 0$ sum-frequency matching [see Eq. (24)], and therefore the power of the negative fifth sideband in the second harmonic is either comparable to or even exceeds the one in the fundamental [see Figs. 10(e) and 10(h), and compare the y-axis scales in Figs. 10(d)–10(f)]. The bottom line in Fig. 10 shows how the Turing patterns loop around the resonator in the reference frame rotating with D_{1f}, so that the most efficient generation of the second harmonic leads to the largest differences between the linear and nonlinear repetition rates, $D_{1f} - D_{1\nu}$ [see the pattern angles in Figs. 10(j)–10(l)].

Figure 11 shows a more global outlook on the frequency conversion processes happening across the PDC tongues when the laser frequency is scanned and its power is fixed, and $\varepsilon_0 > 0$. The stable Turing combs are typically generated for the relatively small intraresonator powers achieved for large positive detunings. When detunings are reduced and the intraresonator powers are increasing the instabilities bring the breather states producing the denser combs as in Figs. 11(f), 11(g) and 11(i), and then more developed chaotic states as in Figs. 11(d) and 11(e).

The difference between the breathers and chaos is further elucidated in Fig. 12. The first and second columns in Fig. 12 compare the spatiotemporal and spatial profiles of the two. The coherence of the breather and the incoherence of the turbulent state are confirmed by comparing the rf spectra of the net powers (third column in Fig. 12), and the per-mode rf spectra (fourth column). The latter shows $|\text{FFT}\{\psi_{\mu f}(t)\}|^2$ plotted vs the mode number, μ, and the rf frequency. The top, i.e., the breather, panel has five visible tilted lines that are vertically separated by the breather period. These are the five subcombs having different offset frequencies.

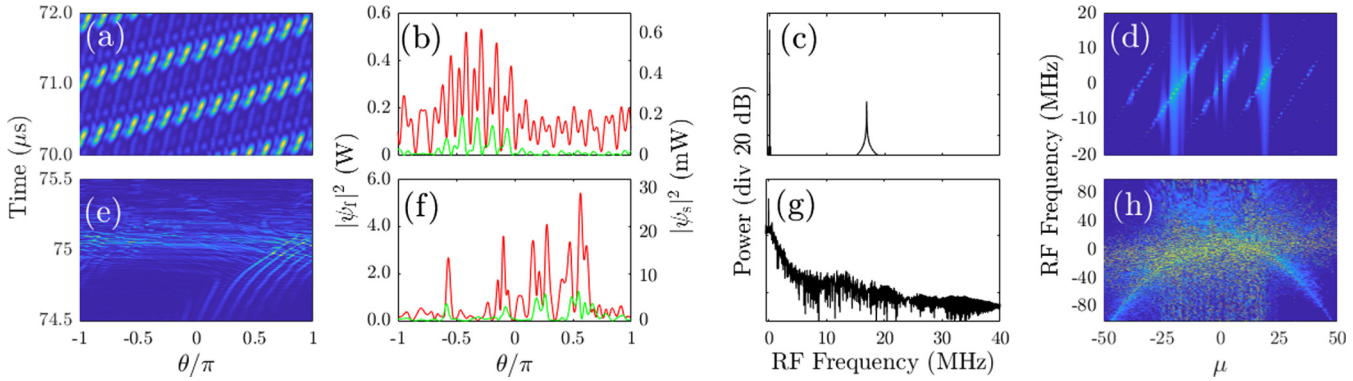

FIG. 12. The top row shows the breather state corresponding to the point "f" in Fig. 11(a). The bottom row is the turbulent state at the point "e" in Fig. 11(a). The first and second columns compare the spatiotemporal dynamics (fundamental) and snapshots of the spatial profiles. The third and fourth columns show the rf spectra of net powers (third), $|\mathrm{FFT}\sum_\mu |\psi_{\mu f}(t)|^2|$, and the per-mode rf spectra (fourth), $|\mathrm{FFT}\{\psi_{\mu f}(t)\}|^2$. One can see that the breather state consists from the five coherent subcombs with the different offsets and the same repetition rates, while the turbulent state shows no mode-locking signs.

In the example shown in the top line of Fig. 12, the maximal parametric gain comes to the sidebands with $\mu = \pm 15$ and to the associated subcombs (see the top panel in the last column), so that the breather could be interpreted as a quasisoliton created via the nondegenerate PDC and dominated by the three groups of modes centered around $\mu = -15, 0, 15$. The power and per-mode rf spectra in the second line of Fig. 12 are unambiguous about the absence of the intermode coherence in the turbulent state. For studies of the transitions between the breather and chaotic states associated with the rogue-wave turbulence in the Kerr resonators, see, e.g., Refs. [59–61].

XII. BRIGHT SOLITON PREREQUISITES

The strong-coupling regime and the dressed state that naturally emerges from it imply that the parametric gain is relatively small, and therefore, to the leading order, the soliton existence problem could be approached through the prism of the nonlinearity vs dispersion balance. In this section, we work through the dispersive and nonlinear properties of the dressed states, and the stability of the cw state that underpins the existence of the bright soliton frequency combs. For normal dispersion, $D_{2\zeta} < 0$, as we have here, these properties suggest the soliton existence for $\varepsilon_0 > 0$, which is the case we describe in detail below. Solitons themselves are introduced in Sec. XIII.

A. Dispersion of dressed states

The microresonator dressed states are parametrized by momentum μ, and represent families of the quasiparticles, photon-photon polaritons, with the effective mass inversely proportional to the polariton dispersion [23]. Our focus here is on the frequency conversion, and therefore the dispersion terminology is more natural. Dispersions of the first and second branches in the dressed spectrum are calculated as

$$\partial_\mu^2 \widetilde{\omega}^{(1)}_{\pm\mu\zeta} = \partial_\mu^2 \beta^{(1)}_{\pm\mu} = \tfrac{1}{2}(D_{2\mathrm{f}} + D_{2\mathrm{s}}) + \tfrac{1}{2}\Omega''_{\pm\mu}, \quad (59a)$$

$$\partial_\mu^2 \widetilde{\omega}^{(2)}_{\pm\mu\zeta} = \partial_\mu^2 \beta^{(2)}_{\pm\mu} = \tfrac{1}{2}(D_{2\mathrm{f}} + D_{2\mathrm{s}}) - \tfrac{1}{2}\Omega''_{\pm\mu}, \quad (59b)$$

where $\Omega''_\mu = \Omega_{\mu+1} + \Omega_{\mu-1} - 2\Omega_\mu$. Ω''_μ depends on $|\Omega|$ (i.e., on the sum-frequency nonlinearity), $D_{2\zeta}$, and on the repetition rate difference, $D_{1\mathrm{f}} - D_{1\mathrm{s}}$, which means that the dressed state dispersion is determined by the interplay of all three factors. This is unlike the bare-state dispersion, trivially given by $\partial_\mu^2 \omega_{\pm\mu\zeta} = D_{2\zeta}$.

For $\varepsilon_0 > 0$, none of the $\widetilde{\omega}^{(1)}_{\mu\zeta}$ frequencies is sum-frequency matched, while $\widetilde{\omega}^{(1)}_{-\mu\zeta}$ are quasimatched for μ around μ_* (see Sec. V and Fig. 5). Therefore, the dressed states corresponding to $\widetilde{\omega}^{(1)}_{\mu\zeta}$ are the quasibare states, $|b^{(1)}_\mu\rangle \approx |1\rangle$, with the dispersion $\approx D_{2\mathrm{f}}$ [see the red line in Fig. 13(a)]. The dressed states corresponding to $\widetilde{\omega}^{(1)}_{-\mu\zeta}$ are $|b^{(1)}_{-\mu}\rangle \approx |3\rangle$ for $\mu < \mu_*$; then, in the proximity of μ_*, they hybridize to the maximally dressed state, $|3\rangle e^{i\phi} - |4\rangle$; and then they transform to the quasibare $|4\rangle$ states.

It is instructive to evaluate the dressed dispersion for μ around μ_*, where $\Delta_{-\mu} \approx 0$, $\Omega_{-\mu} \approx |\Omega|$ [see Eqs. (16) and (17)]:

$$\Omega''_{-\mu} \approx \frac{\Delta^3_{-\mu}\Delta''_{-\mu} + |\Omega|^2(\Delta'_{-\mu}\Delta_{-\mu})'}{\Omega^3_{-\mu}} \approx \frac{(\Delta'_{-\mu})^2}{|\Omega|} \approx \frac{(D_{1\mathrm{f}} - D_{1\mathrm{s}})^2}{|\Omega|} \sim 1 \text{ to } 10 \text{ GHz}. \quad (60)$$

The above strongly dominates over $D_{2\zeta}$, so that the dispersion of $\widetilde{\omega}^{(1)}_{-\mu\zeta}$ becomes largely anomalous. Thus, dressing the $\widetilde{\omega}^{(1)}_{-\mu\zeta}$ branch creates two zero dispersion points around μ_* and puts a group of modes into the range of anomalous dispersion [see Fig. 13(a)].

The dressing induced dispersion changes are very large [see Eq. (60)], so that for the nonlinearity to compensate the dispersive pulse spreading it would be preferential to engage the modes with the bare resonator dispersion around $\mu = 0$, and away from μ_*. Thus keeping $\mu_* \gg 1$ and increasing it by tuning the index to make $|\varepsilon_0|$ larger [see Eq. (30)] is expected to increase the bandwidth of modes suitable for the bright soliton mode-locking regime.

In other words, the repetition rate difference can be large, but the sum-frequency matching to the appropriately large

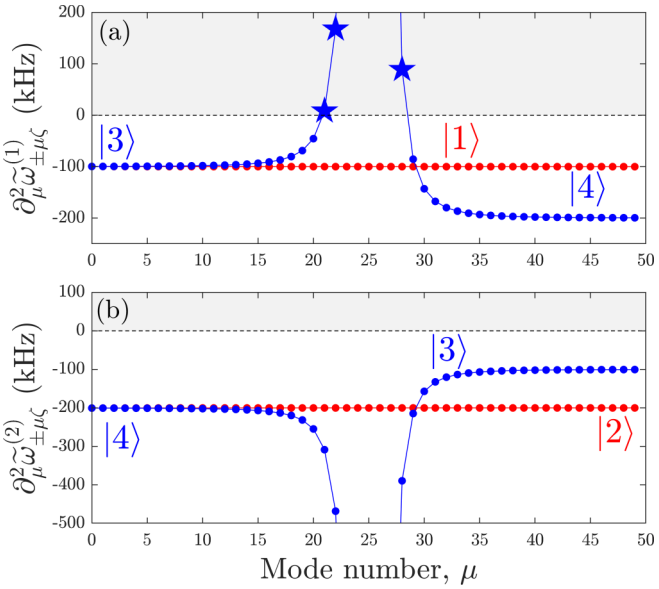

FIG. 13. Dispersion of the dressed states [see Eq. (59)], normalized to 2π: (a) $\widetilde{\omega}^{(1)}_{\pm\mu\zeta}$ and (b) $\widetilde{\omega}^{(2)}_{\pm\mu\zeta}$. The red lines correspond to the positive sidebands, $\widetilde{\omega}^{(1),(2)}_{\mu\zeta}$, and the blue ones correspond to the negative sidebands, $\widetilde{\omega}^{(1),(2)}_{-\mu\zeta}$. The values of -100 and -200 kHz are the values of $D_{2\mathrm{f}}$ and $D_{2\mathrm{s}}$ in the bare resonator. The gray shading and stars show the dressed states with the anomalous dispersion induced by the dressing. In (a), the maximal anomalous dispersion of $\approx$1 GHz (not shown) is achieved at $\mu = 25$ for the $|b^{(3)}_{25}\rangle \approx |3\rangle e^{i\phi} - |4\rangle$ state. Parameters are $|\Omega|/2\pi = 116$ MHz, $\varepsilon_0/2\pi = 25$ GHz, $\delta = -3.8\kappa_{\mathrm{f}}$.

sideband number puts the undesirably large dispersion this difference creates away from the spectral core of the soliton.

B. Optical Pockels and cascaded-Kerr nonlinearities

Since we are expecting to work with the normal dispersion, the bright solitons would require the negative, i.e., defocusing, nonlinearity to compensate for it. Derivatives of $\widetilde{\omega}^{(j)}_{\pm\mu\zeta}$ in $|\Omega|$ describe the rate of the nonlinear shifts of the frequencies in the dressed spectrum with the intraresonator power:

$$\frac{\partial\widetilde{\omega}^{(1)}_{\pm\mu\zeta}}{\partial|\Omega|} = \frac{1}{2}\frac{\partial\Omega_{\pm\mu}}{\partial|\Omega|} = \frac{|\Omega|}{2\Omega_{\pm\mu}} > 0,$$
$$\frac{\partial\widetilde{\omega}^{(2)}_{\pm\mu\zeta}}{\partial|\Omega|} = -\frac{|\Omega|}{2\Omega_{\pm\mu}} < 0. \tag{61}$$

The signs of the above expressions determine the signs of the effective nonlinearities experienced by the sidebands. Since the resonator frequencies are inversely proportional to the refractive index [see Eq. (9)], we conclude that the frequencies $\widetilde{\omega}^{(2)}_{\pm\mu\zeta}$ in the dressed spectrum experience the net positive (self-focusing) nonlinearity, and $\widetilde{\omega}^{(1)}_{\pm\mu\zeta}$ experience the net negative (defocusing) nonlinearity.

Though the branch nonlinearities do not change signs, their dependence on $|\Omega|$ varies profoundly. Indeed, $\Omega_{\pm\mu}$ admits two qualitatively different Taylor series expansions (see Table II):

$$\Omega_{\pm\mu} = |\Omega| + \frac{\Delta^2_{\pm\mu}}{2|\Omega|} + \ldots, \quad \frac{\Delta^2_{\pm\mu}}{|\Omega|^2} \ll 1, \tag{62a}$$
$$\Omega_{\pm\mu} = |\Delta_{\pm\mu}| + \frac{|\Omega|^2}{2|\Delta_{\pm\mu}|} + \ldots, \quad \frac{\Delta^2_{\pm\mu}}{|\Omega|^2} \gg 1. \tag{62b}$$

Thus, if μ is near to μ_*, then the nonlinear shift of $\widetilde{\omega}^{(j)}_{\pm\mu\zeta}$ frequency is proportional to the amplitude of the cw state, $|\Omega| \sim |\psi_{\mathrm{f}}|$, which corresponds to the optical Pockels effect [see Eq. (62a)], while, for μ away from μ_*, the nonlinear shifts are proportional to the power, $|\Omega|^2 \sim |\psi_{\mathrm{f}}|^2$, and hence are Kerr-like, i.e., correspond to the cascaded-Kerr effect [see Eq. (62b)].

C. Cw-state stability and instability

From the above, one should conclude that, for $\varepsilon_0 > 0$, the first branch of the dressed states should be considered as the one able to form the bright solitons, since it provides a

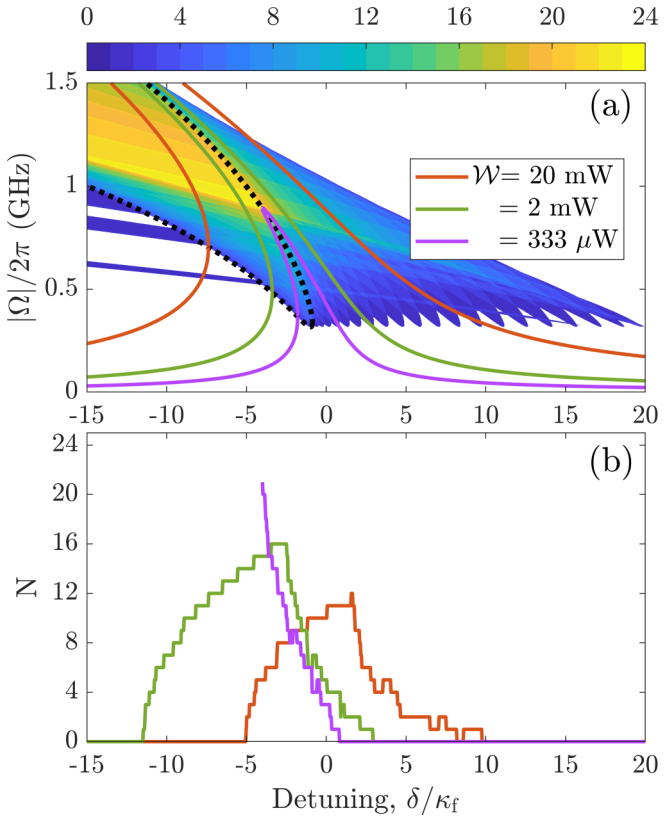

FIG. 14. (a) Parametric instability tongues in the $(\delta, |\Omega|)$ plane, for $\varepsilon_0/2\pi = 25$ GHz [see $\varepsilon_0/2\pi = 5$ GHz in Fig. 9(a)]. The colorbar shows the number of the simultaneously unstable sidebands, N. The black dotted line embraces the $\mu = 0$ instability range, i.e., the middle branch of the bistability loop. N is clamped by $\mu_* = |\varepsilon_0|/|D_{1\mathrm{f}} - D_{1\mathrm{s}}| = 25$, $N \leqslant \mu_*$. (b) N vs δ for three values of $\mathcal{W}$ (laser power) computed along the upper branch of the cw state. The magenta line ($\mathcal{W} = 333$ μW) terminates at the tip of the cw resonance, i.e., at the end of the bistability range. The other two lines are for the higher powers and terminate before the tip, thereby marking stabilization of the cw state.

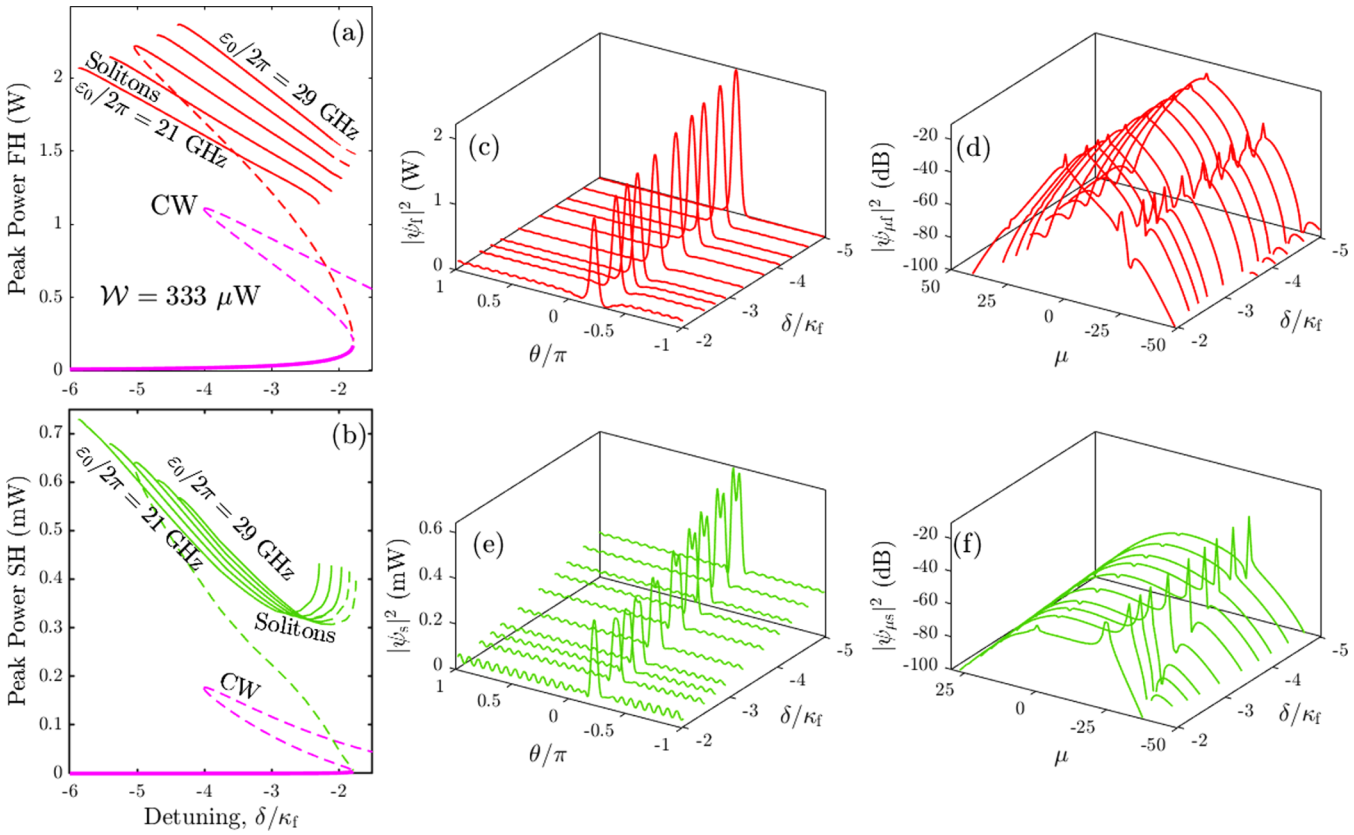

FIG. 15. Families of the bright solitons computed for the laser power $\mathcal{W} = 333\ \mu$W and plotted vs δ. The first line data show the fundamental field, and the second line is for the second harmonic. (a, b) Soliton branches (red and green lines) and the cw state (magenta lines) vs δ. The solitons are shown for a range of frequency mismatch parameters, $\varepsilon_0/2\pi = 21$, 23, 25, 27, and 29 GHz. The full lines correspond to the stable solutions, and the dashed lines correspond to the unstable ones. The $\varepsilon_0/2\pi = 25$ GHz case in (a) and (b) is the one that shows how the unstable soliton splits from the cw state and then connects to the stable soliton. (c, e) How the spatial profile of the soliton changes with δ for $\varepsilon_0/2\pi = 25$ GHz. (d, f) Like (c) and (e) but showing the envelopes of the discrete soliton spectra (see Fig. 17).

combination of the defocusing nonlinearity and the relatively small normal dispersion, except several μ's around μ_*, where dispersion is anomalous.

The same condition, as the one just stated, leads to the intrabranch instability of the cw state [see and compare Fig. 9(a) for $\varepsilon_0/2\pi = 5$ GHz and Fig. 14(a) for $\varepsilon_0/2\pi = 25$ GHz]. Recalling the results of Sec. VII [see Eq. (47)], the number, N, of the sidebands that can be simultaneously unstable under these conditions is clamped by μ_*. Therefore, and also in line with the previous subsection, $\varepsilon_0/2\pi = 25$ GHz brings more of the unstable sidebands. Figure 14 shows that there exists the optimal laser power, $\mathcal{W}$, achieving the maximal N.

N going up and then down with δ tuned more negative and powers increasing [see Fig. 14(b)] is due to the nonlinear shifts becoming saturated by the higher-order terms in the expansions of the root function in $\Omega_{\pm\mu}$. The weakened nonlinear shifts gradually bring the parametric gain below the threshold first for some and finally for all the sidebands. The N vs δ dependencies in Fig. 14(b) would be very different in the Kerr resonators, where the number of the unstable sidebands tends to infinity with the simultaneous increases of δ and $\mathcal{W}$ [46].

It is now important to note that, for $\delta < 0$, the above discussed instabilities happen to the upper state of the cw bistability loop, while the low branch is either exclusively or largely stable [see Figs. 14(a) and 15(a)]. The stable low-amplitude cw state makes the background for the bright solitons reported in the next section.

XIII. BRIGHT SOLITON FREQUENCY COMBS

The results of the previous section allow us to conclude that, for the normal dispersion of the bare resonator modes, $D_{2\zeta} < 0$, the bright solitons are expected provided one arranges the index (frequency) matching parameter between the M and $2M$ resonator modes to be positive,

$$\varepsilon_0 \sim (n_{2M} - n_M) > 0, \tag{63}$$

and sufficiently large, so that the sum-frequency matching or near matching,

$$\omega_{0f} + \omega_{-\mu f} - \omega_{-\mu s} = 0, \tag{64}$$

happens for

$$\mu = \mu_* \gg 1. \tag{65}$$

The detuning should than be tuned to $\delta < 0$, i.e., "blue" detuning. μ_* is well approximated by the ratio between $|\varepsilon_0|$ and the repetition rate difference, $|D_{1f} - D_{1s}|$ [see Eq. (30)].

We now do as prescribed and select the laser power, $\mathcal{W}$, and detuning, δ, corresponding to a large number of the simulta-

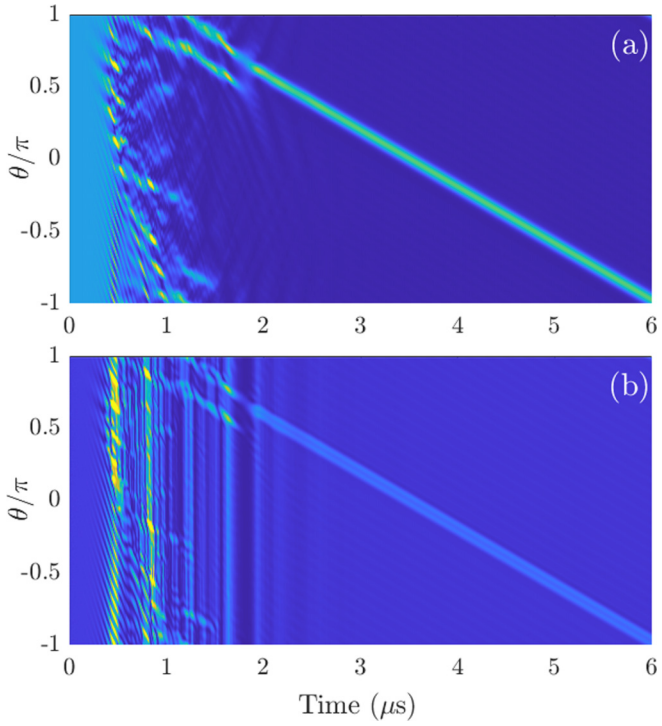

FIG. 16. Instability of the cw state and spontaneous birth of the bright soliton. Laser power $\mathcal{W} = 333\ \mu$W, $\varepsilon_0/2\pi = 25$ GHz, and $\delta = -3.8\kappa_\mathrm{f}$. (a) Fundamental field. (b) Second harmonic.

neously unstable sidebands (see Fig. 14). Initializing Eq. (A1) with the cw state we immediately observe its instability and the subsequent formation of the stable two-color soliton (see Fig. 16).

For $D_{2\zeta} > 0$ (anomalous dispersion), the bright solitons would require $\varepsilon_0 < 0$, adjusting $\omega_{0\mathrm{f}} + \omega_{\mu\mathrm{f}} - \omega_{\mu\mathrm{s}} = 0$ for $\mu = \mu_* \gg 1$, and, then, tuning to $\delta > 0$, i.e., "red" detuning. The mixed dispersion case, $D_{2\mathrm{f}}D_{2\mathrm{s}} < 0$, requires a separate analysis.

To trace the soliton families in the parameter space we solve the comb equations in Sec. X. Since the teeth of the single soliton combs follow with step 1, i.e., their spatial period is 2π, we set $\nu = 1$ in Eqs. (55) and (57). Families of the bright solitons traced in δ for the laser power $\mathcal{W} = 333\ \mu$W and for a range of frequency mismatch parameters, $\varepsilon_0/2\pi \in [21, 29]$ GHz, are shown in Fig. 15. The unstable soliton branch (dashed red and green lines) splits from the middle branch of the cw state (dashed magenta lines) at the point of its $\mu = 1$ instability. The stable soliton branches extend outside the cw bistability towards more negative δ's.

The soliton profiles along the resonator circumference shown in Figs. 15 and 17 are characterized by the tails oscillating with the period $2\pi/\mu_*$. The corresponding spectra have pronounced peaks at $\mu = -\mu_*$, where the powers of the fundamental and second-harmonic sidebands are balanced due to the sum-frequency matching. The background of the soliton in the fundamental field is set primarily by the $\mu = 0$ sideband [see spectra in Fig. 15(d)], where $\mu = 0$ is stronger than $\mu = -\mu_*$. Therefore, the fundamental background drops with δ becoming more negative [see the correlated changes of the full cw line in Fig. 15(a) and of the soliton background in Fig. 15(c)]. The background of the soliton in the second harmonic is, however, set primarily by the $\mu = -\mu_*$ sideband [see spectra in Fig. 15(f)], where $\mu = -\mu_*$ is the strongest and its power correlates with the soliton peak power. This explains why the second-harmonic soliton background goes up with δ becoming more negative [see the dropping full cw line in Fig. 15(b) and the increasing soliton background in Fig. 15(e)].

The oscillatory soliton tail should be interpreted as due to the inability of the nonlinear effects to compensate for the sharp rise and the sign change of the dressed state dispersion around μ_* (see Fig. 13). Therefore, the nature of the tails here is similar to the soliton Cherenkov radiation in the resonators [40,62,63], fibers [64], and bulk crystals [65]. We note that, in the present case, the dispersion can be significantly altered by the pump power dependent state dressing, which provides a more flexible tool to control the radiation frequency.

Figure 17 shows how the soliton families change with the tuning of ε_0. Here the structure of the families appears to be more complex. The period of the oscillations of the soliton tail, $2\pi/\mu_*$, can change only discretely while $|\varepsilon_0|$ is tuned continuously, so that the solution is forced to accommodate itself, as much as it can, to the rigid period of its tails, which leads to the discrete set of the soliton families. Each family is centered around the value of $|\varepsilon_0| = \mu_*|D_{1\mathrm{f}} - D_{1\mathrm{s}}|$; we recall that $|D_{1\mathrm{f}} - D_{1\mathrm{s}}|/2\pi = 1$ GHz. The tail oscillations of the Kerr solitons in microresonators with the large higher-order dispersions also lead to somewhat similar "quantized" behavior of the soliton parameters [47].

XIV. DISCUSSION

There are numerous open problems left for a researcher tempted to understand the multimode dynamics of the high-Q $\chi^{(2)}$ microresonators by looking into properties of the individual modes, in line with the present-day experimental capabilities. The extension of our results to the case of the exact index matching $\varepsilon_0 = 0$ while keeping $D_{1\mathrm{f}} - D_{1\mathrm{s}}$ large requires separate consideration. Extending the bandwidth of the soliton combs by taking the shorter resonators with the higher repetition rates and lower quality factors and, perhaps, larger μ_* needs to be investigated.

The power induced dispersion engineering of the dressed states offers a method to control the comb widths and shapes. Further work on the solitons and Rabi splitting is of course important and can be performed with the currently available resonators and index matching control tools. We note the relatively high conversion efficiency from the pump to the soliton-comb spectra seen in Fig. 17, which could be an important practical aspect requiring further exploration.

We should recall here the prior theoretical work on the spatial [55,57] and temporal [30,38] resonator solitons achieved via the second-harmonic generation arrangements requiring the exactly or near matched phase, $\varepsilon_0 = 0$, and group, $D_{1\mathrm{f}} = D_{1\mathrm{s}}$, velocities. While a combination of these assumptions appears as the desirable idealization in the contexts of the currently available ring microresonators, future studies along these lines are warranted. The relevance of the strong-coupling and dressed states for the microres-

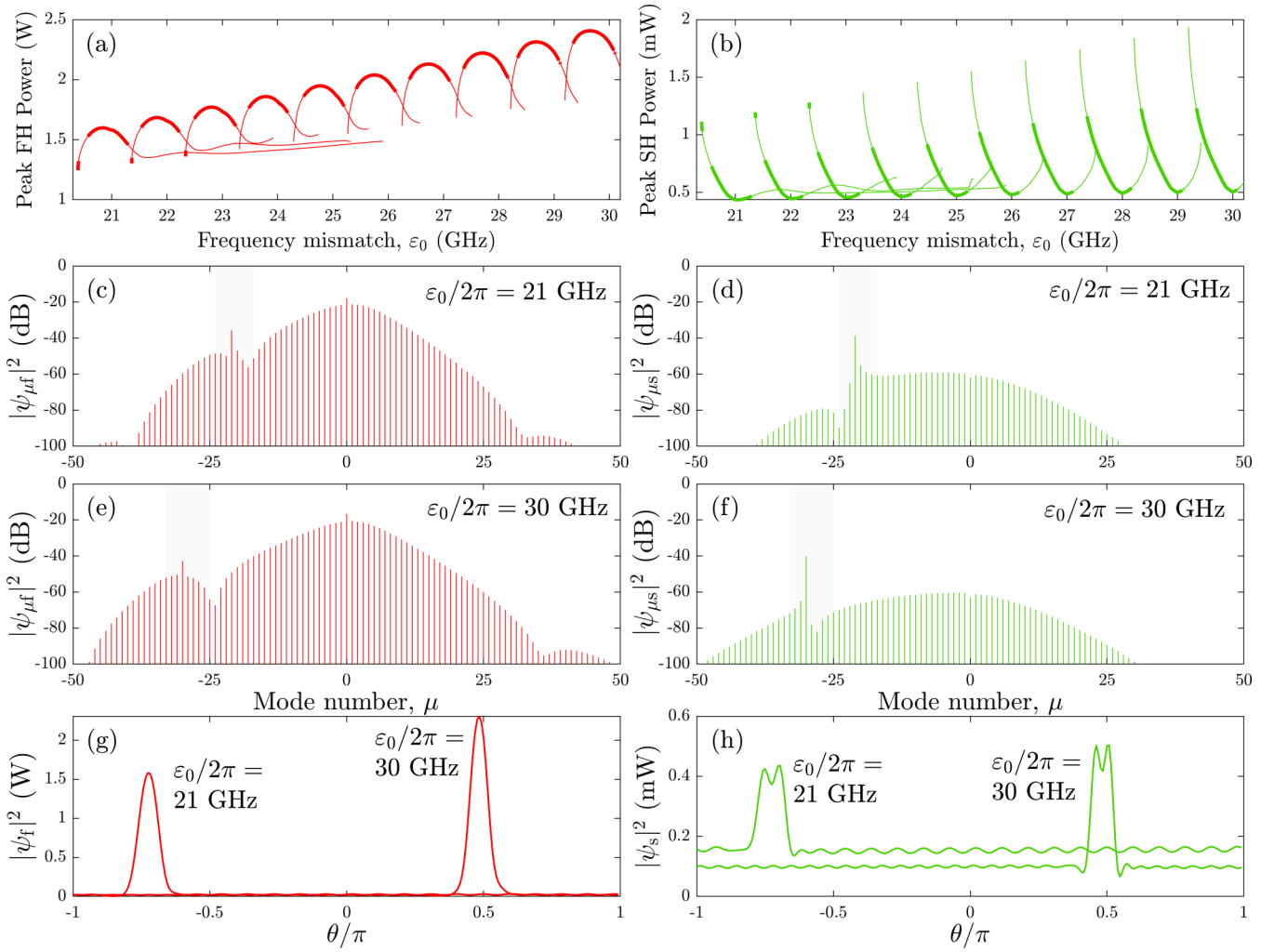

FIG. 17. Families of the bright solitons computed for the laser power $\mathcal{W} = 333$ μW and plotted vs ε_0 for $\delta = -3.9\kappa_f$. The first and second columns show the fundamental and second-harmonic data, respectively. (a, b) Multiple soliton branches centered around $\varepsilon_0/2\pi \approx \mu_*$ [see Eq. (30)]. (c–f) Spectra at the indicated values of ε_0. (g, i) Respective spatial soliton profiles. The shaded areas in (c)–(f) highlight the interval between the two zero dispersion points (see Fig. 13).

onator half-harmonic generation arrangement remains to be analyzed, including their links to the results on the half-harmonic bright-bright, dark, and dark-bright soliton pulses [15,27,31,58,66–69].

XV. SUMMARY

(1) The theoretical framework, i.e., dressed-resonator method, to study frequency conversion and solitons is formulated by including the sum-frequency nonlinearity into the definition of the resonator spectrum.

(2) The Rabi splitting of the dressed frequencies leads to the four distinct PDC conditions [see Eq. (43)], which are used to explain the existence and generation of the sparse nonsoliton, i.e., Turing-pattern-like, frequency combs.

(3) The effective nonlinearity and dispersion of the dressed states have been used to demonstrate that the microresonator with the normal dispersion and naturally large difference of the repetition rates at the fundamental and second-harmonic frequencies, $D_{1f} - D_{1s}$, supports a family of the bright soliton frequency combs (see Figs. 15 and 17). Conditions for this are provided by tuning the index and frequency matching parameter, $\varepsilon_0 = 2\omega_{0f} - \omega_{0s}$, to be positive and large, so that it exceeds the repetition rate difference by a significant factor, $\mu_* = |\varepsilon_0|/|D_{1f} - D_{1s}| \gg 1$. μ_* and $-\mu_*$ approximate the mode number associated with the phase-matched sum-frequency process and set limits on the soliton bandwidth.

ACKNOWLEDGMENT

This work was supported by the European Union Horizon 2020 Framework Programme (MICROCOMB Grant No. 812818).

APPENDIX A: ENVELOPE EQUATIONS

The intraresonator electric fields of the fundamental and second harmonic are expressed as per Eq. (2). Envelopes of

the fundamental, $\psi_{\rm f}$, and second, $\psi_{\rm s}$, harmonic satisfy the following system of partial-differential equations:

$$i\partial_t\psi_{\rm f} = \delta\psi_{\rm f} - iD_{1\rm f}\partial_\vartheta\psi_{\rm f} - \tfrac{1}{2}D_{2\rm f}\partial_\vartheta^2\psi_{\rm f} - \gamma_{\rm f}\psi_{\rm s}\psi_{\rm f}^* - \mathcal{N}_{\rm f} - i\tfrac{1}{2}\kappa_{\rm f}(\psi_{\rm f} - \mathcal{H}), \tag{A1a}$$

$$i\partial_t\psi_{\rm s} = (2\delta - \varepsilon_0)\psi_s - iD_{1\rm s}\partial_\vartheta\psi_{\rm s} - \tfrac{1}{2}D_{2\rm s}\partial_\vartheta^2\psi_{\rm s} - \gamma_{\rm s}\psi_{\rm f}^2 - \mathcal{N}_{\rm s} - i\tfrac{1}{2}\kappa_{\rm s}\psi_{\rm s}. \tag{A1b}$$

Conditions $\psi_\zeta(t,\vartheta) = \psi_\zeta(t,\vartheta+2\pi)$ make this system equivalent to a set of coupled-mode equations for $\psi_{\mu\zeta}(t)$. The first-principle derivation of Eq. (A1) is given in Ref. [29].

All parameters are explained in Sec. III of the main text, apart from $\mathcal{H}^2$, which characterizes the pump power [29]. If $\mathcal{F} = D_{1\rm f}/\kappa_{\rm f} = 20\,000$ is the finesse, then $\mathcal{H}^2$ is expressed via the incoming laser power $\mathcal{W}$ as

$$\mathcal{H}^2 = \frac{\eta}{\pi}\mathcal{F}\mathcal{W}. \tag{A2}$$

$\eta < 1$ is the coupling efficiency. $\mathcal{N}_\zeta$ are the intrinsic Kerr, i.e., $\chi^{(3)}$, nonlinearity terms:

$$\mathcal{N}_{\rm f,s} = \gamma_{3\rm f,3s}(|\psi_{\rm f,s}|^2 + 2|\psi_{\rm s,f}|^2)\psi_{\rm f,s}. \tag{A3}$$

Nonlinear coefficients $\gamma_\zeta/2\pi$ and $\gamma_{3\zeta}/2\pi$ have units of Hz/$\sqrt{[b]\text{W}}$ and Hz/W, respectively [29]. Units and numerical values of other parameters can be found in Table I.

APPENDIX B: CW STATE: $\chi^{(2)}$ VS $\chi^{(3)}$

The cw state, i.e., the $\mu = 0$ mode in the fundamental and its second harmonic, is a solution of Eqs. (A1) with $\psi_\zeta = \psi_{0\zeta}$, $\partial_\vartheta\psi_{0\zeta} = \partial_t\psi_{0\zeta} = 0$. Let us now evaluate the relative impact of the $\chi^{(2)}$ and $\chi^{(3)}$ effects on the cw state. If ε_0 dominates over the linewidth and detuning parameters, then $\psi_{0\rm s} \approx -\gamma_{\rm s}\psi_{0\rm f}^2/\varepsilon_0$, and the net nonlinear frequency shift of the fundamental resonance is

$$\left[-\frac{\gamma_{\rm s}\gamma_{\rm f}}{\varepsilon_0} + \gamma_{3\rm f}\right]|\psi_{0\rm f}|^2 = \gamma_{3\rm f}\left[-\frac{\varepsilon_{\rm cr}}{\varepsilon_0} + 1\right]|\psi_{0\rm f}|^2. \tag{B1}$$

Hence, only for $|\varepsilon_0| \gtrsim |\varepsilon_{\rm cr}|$, $\varepsilon_{\rm cr} = \gamma_{\rm s}\gamma_{\rm f}/\gamma_{3\rm f}$, the second harmonic becomes weak enough for the $\chi^{(3)}$ induced shift to catch up with the $\chi^{(2)}$ one. For the parameters in Table I and $\gamma_{3\zeta}/2\pi \simeq 1$ MHz/W [29], $\varepsilon_{\rm cr}/2\pi \simeq 100$ GHz, i.e., in order for the $\chi^{(3)}$ effects to make the impact on the cw solutions as $\chi^{(2)}$, the $2\omega_p$ photon should miss the resonator frequency providing the exact frequency matching by more than five free spectral ranges. Thus, in the range of $\varepsilon_0/2\pi \in [-30, 30]$ GHz explored in this project and for the combs with the relatively low powers, the $\chi^{(3)}$ terms can be neglected. However, most of the numerical data in this paper have been calculated with and without $\mathcal{N}_\zeta$. The differences that we have observed are not worth mentioning in the context of our paper. For all the above reasons, we set $\mathcal{N}_\zeta = 0$ in this paper. Some results on the interplay of the $\chi^{(2)}$ and $\chi^{(3)}$ effects in the half-harmonic generation setup can be found in, e.g., Refs. [15,31].

APPENDIX C: CW STATE: $\chi^{(2)}$ ONLY

The cw state is sought in the form

$$\psi_{0\rm f} = \frac{\Omega}{\sqrt{2\kappa_{\rm f}\kappa_{\rm s}}}\mathcal{H}_*,\ \psi_{0\rm s} = \frac{8\gamma_{2\rm s}\psi_{0\rm f}^2}{\Omega_{\rm s}} = \frac{\Omega^2}{\gamma_{2\rm f}\Omega_{\rm s}}, \tag{C1}$$

where Ω is the Rabi frequency. $\Omega_{\rm s}$ is defined in Eq. (19), and

$$\mathcal{H}_*^2 = \frac{\kappa_{\rm f}\kappa_{\rm s}}{4\gamma_{2\rm f}\gamma_{2\rm s}} \approx 30\ \mu\text{W} \tag{C2}$$

is the characteristic intraresonator power. Thus, the explicit relation between the Rabi frequency and the power in the fundamental field is

$$|\psi_{0\rm f}|^2 = \frac{|\Omega|^2}{8\gamma_{2\rm f}\gamma_{2\rm s}}. \tag{C3}$$

Using Eqs. (A1), one can show that

$$\Omega = \sqrt{\frac{\kappa_{\rm f}\kappa_{\rm s}}{2}}\sqrt{\frac{\mathcal{W}}{\mathcal{W}_*}}\frac{\kappa_{\rm f}}{\Omega_{\rm f}}\left[1 - \frac{|\Omega|^2}{\Omega_{\rm f}\Omega_{\rm s}}\right]^{-1}. \tag{C4}$$

Here, $\Omega_{\rm f,s}$ are defined after Eq. (49), and

$$\mathcal{W}_* = \frac{\pi\mathcal{H}_*^2}{\eta\mathcal{F}} \approx 10\ \text{nW}. \tag{C5}$$

Taking the modulus squared of Eq. (C4) we find the real cubic equation for $|\Omega|^2$:

$$\frac{2|\Omega_{\rm f}|^2|\Omega|^2}{\kappa_{\rm f}^3\kappa_{\rm s}} \times \left[1 - |\Omega|^2\text{Re}\left\{\frac{2}{\Omega_{\rm f}\Omega_{\rm s}}\right\} + \frac{|\Omega|^4}{|\Omega_{\rm f}|^2|\Omega_{\rm s}|^2}\right] = \frac{\mathcal{W}}{\mathcal{W}_*} = \frac{\mathcal{H}^2}{\mathcal{H}_*^2}. \tag{C6}$$

A useful insight into the cw properties is provided by taking the limit when $|\varepsilon_0|$ is large relative to $|\delta|$, and $|\delta|$ is large relative to κ_ζ, so that $\Omega_{\rm s} \approx -8\varepsilon_0$ and $\Omega_{\rm f} \approx \delta$. Then, bistability of the cw state requires $\delta\varepsilon_0 < 0$ [the square bracket in Eq. (C4) can be zero]. In this regime,

$$\max_\delta |\Omega|^2 \simeq -\delta\varepsilon_0, \tag{C7}$$

implying that the resonance shifts proportionally to the pump power, i.e., in the same way as it happens in Kerr effect. This means that the cw state behaves as it would in the Kerr resonator. For $\varepsilon_0 = 0$ or smaller, $\Omega_{\rm f} \approx \delta$, $\Omega_{\rm s} \approx 16\delta$. Then, the cw becomes simultaneously bistable for $\delta > 0$ and $\delta < 0$ [30,38], and $\max_\delta |\Omega|^2 \simeq \delta^2$, i.e.,

$$\max_\delta |\Omega| \simeq |\delta|. \tag{C8}$$

This is the Pockels regime of the cw state, when the nonlinear change of the refractive index is proportional to the first power of the field amplitude, which we do not consider in this paper. Conditions for the $\mu \neq 0$ sidebands to be in either cascaded-Kerr or Pockels regimes are different and discussed in Sec. XII B.

APPENDIX D: LINEARIZATION AROUND THE CW STATE

In order to develop a theory of the growth of the multisideband signal, i.e., frequency comb, on top of the cw solution, $\psi_{0\zeta}$, we extend Eqs. (A1) by a pair of the complex-conjugated

equations [70], and seek a solution in the form

$$\begin{bmatrix}\psi_{\rm f}\\ \psi_{\rm s}\\ \psi_{\rm f}^*\\ \psi_{\rm s}^*\end{bmatrix}=\begin{bmatrix}\psi_{0\rm f}\\ \psi_{0\rm s}\\ \psi_{0\rm f}^*\\ \psi_{0\rm s}^*\end{bmatrix}+\sum_{\mu\geqslant 0}\left\{\begin{bmatrix}\widetilde{\psi}_{\mu\rm f}\\ \widetilde{\psi}_{\mu\rm s}\\ \widetilde{\psi}_{-\mu\rm f}\\ \widetilde{\psi}_{-\mu\rm s}\end{bmatrix}e^{i\mu\theta}+\begin{bmatrix}0&0&1&0\\ 0&0&0&1\\ 1&0&0&0\\ 0&1&0&0\end{bmatrix}\begin{bmatrix}\widetilde{\psi}_{\mu\rm f}^*\\ \widetilde{\psi}_{\mu\rm s}^*\\ \widetilde{\psi}_{-\mu\rm f}^*\\ \widetilde{\psi}_{-\mu\rm s}^*\end{bmatrix}e^{-i\mu\theta}\right\}. \tag{D1}$$

If ϑ is the angle measured along the resonator circumference, then $\theta=\vartheta-D_1t$ is the coordinate in the rotating frame [see Eq. (6)]. $\widetilde{\psi}_{\pm\mu\zeta}(t)$ are the sideband amplitudes. Summing up the first and second lines gives the net signals in the fundamental and second harmonic, respectively, with the third and fourth lines being their conjugations [see Eq. (11)]. Substituting Eq. (D1) into the extended Eq. (A1), we assume smallness of the sideband amplitudes, linearize, and then derive equations for the individual sidebands using the angular momentum matching. For a given μ this leads to a coupled system of the four ordinary differential equations for $\widetilde{\psi}_{\mu\rm f}$, $\widetilde{\psi}_{-\mu\rm f}$, $\widetilde{\psi}_{\mu\rm s}$, and $\widetilde{\psi}_{-\mu\rm s}$ [see Eq. (12)].

APPENDIX E: APPROXIMATE PDC CONDITIONS

To present the PDC condition in Eq. (45) in a more transparent form, we first make explicit how δ, ε_0, and μ_* are implicated there:

$$\begin{aligned}|\Omega_{\rm pdc}|^2=&\frac{4}{[(\delta-\delta_{\mu\rm f})+(2\delta-\delta_{\mu\rm s}-\varepsilon_0)]^2}\\ &\times(\delta-\delta_{\mu\rm f})\\ &\times(2\delta-\delta_{\mu\rm s}-\varepsilon_0)\\ &\times\left[3\delta-\delta_{\mu\rm s}-\delta_{\mu\rm f}-\varepsilon_0\left(1+\frac{\mu}{\mu_*}\right)\right]\\ &\times\left[3\delta-\delta_{\mu\rm s}-\delta_{\mu\rm f}-\varepsilon_0\left(1-\frac{\mu}{\mu_*}\right)\right],\end{aligned} \tag{E1}$$

where we have defined

$$\delta_{\mu\rm f}=-\tfrac{1}{2}D_{2\rm f}\mu^2,\ \delta_{\mu\rm s}=-\tfrac{1}{2}D_{2\rm s}\mu^2. \tag{E2}$$

Equation (21) implies that $|\varepsilon_0|$ dominates over all δ's. The first case to consider is when μ_* falls between the two nearest integers, i.e., the sum-frequency matching point $\mu=\mu_*$ has been missed. Then Eq. (E1) simplifies to Eq. (46):

$$|\Omega_{\rm pdc}|^2\approx-4\varepsilon_0(\delta-\delta_{\mu\rm f})\left[1-\frac{\mu^2}{\mu_*^2}\right]. \tag{E3}$$

If the sum-frequency process is either nearly or exactly matched at

$$\mu=\widehat{\mu}\approx\mu_*,\quad\text{where}\quad\widehat{\mu}\in\mathbb{Z},\,\mu_*\in\mathbb{R}, \tag{E4}$$

then

$$\left|\Omega_{\rm pdc}^{(\widehat{\mu})}\right|^2\approx 8(\delta-\delta_{\widehat{\mu}\rm f})(3\delta-\delta_{\widehat{\mu}\rm s}-\delta_{\widehat{\mu}\rm f}). \tag{E5}$$

Transition from Eq. (E3) to Eq. (E5) implies transition from the square-root (Kerr-like) dependence of $|\Omega_{\rm pdc}|$ vs δ to the quasilinear (Pockels-like) one.

APPENDIX F: LASER POWER AT THE PDC THRESHOLDS

Detunings at the tips of the instability tongues are worked out by imposing conditions

$$\left|\Omega_{\rm pdc}\right|^2=\left|\Omega_{\rm th}^{(\mu)}\right|^2, \tag{F1a}$$

$$\left|\Omega_{\rm pdc}^{(\widehat{\mu})}\right|^2=\left|\Omega_{\rm th}^{(\widehat{\mu})}\right|^2. \tag{F1b}$$

Equations (F1a), (46), and (52) yield

$$\delta_{\rm th}^{(\mu)}=\delta_{\mu\rm f}-\frac{\kappa_{\rm f}{\rm sgn}(\varepsilon_0)}{1-\frac{\mu^2}{\mu_*^2}},\quad\mu\neq\widehat{\mu}. \tag{F2}$$

For $\mu=\widehat{\mu}$, the procedure is the same. In order not to overcomplicate the answer, we impose a plausible condition $(D_{2\rm f}+D_{2\rm s})=3D_{2\rm f}$, leading to $\delta_{\widehat{\mu}\rm s}+\delta_{\widehat{\mu}\rm f}=3\delta_{\widehat{\mu}\rm f}$. Then, Eqs. (F1b), (E5), and (53) yield

$$\delta_{\rm th}^{(\widehat{\mu})}=\delta_{\widehat{\mu}\rm f}\pm\sqrt{\frac{|\varepsilon_0|}{6}\sqrt{\kappa_{\rm f}(\kappa_{\rm f}+\kappa_{\rm s})}}. \tag{F3}$$

Transparent analytic estimates for the laser powers $\mathcal{W}$ at the tips of the instability tongues can be worked out after observing that along the tails of the nonlinear resonances (see Fig. 2) the square bracket in Eq. (C4) is $\approx$1:

$$\frac{\mathcal{W}}{\mathcal{W}_*}\approx\frac{2\delta^2|\Omega|^2}{\kappa_{\rm f}^3\kappa_{\rm s}} \tag{F4}$$

[see Eq. (C5) for $\mathcal{W}_*$].

The balance of terms in Eq. (F3) is such that the root term dominates and $\delta_{\widehat{\mu}\rm f}$ can be neglected, which gives the following estimate for the power:

$$\frac{\mathcal{W}_{\rm th}^{(\widehat{\mu})}}{\mathcal{W}_*}\approx\frac{4|\varepsilon_0|^2(\kappa_{\rm f}+\kappa_{\rm s})}{3\kappa_{\rm f}^2\kappa_{\rm s}},\,\mu=\widehat{\mu}. \tag{F5}$$

In Eq. (F2), the two terms are balanced for the moderate μ's leading to a longer equation not included here, but for $\mu^2\gg\mu_*^2$ the second term can be neglected, so that

$$\frac{\mathcal{W}_{\rm th}^{(\mu)}}{\mathcal{W}_*}\approx 2\mu^4\frac{D_{2\rm f}^2|\varepsilon_0|}{\kappa_{\rm f}^2\kappa_{\rm s}},\,\mu\gg\mu_*. \tag{F6}$$

Thus, the powers to generate the sum-frequency matched sideband, $\mu=\widehat{\mu}$, scale with $|\varepsilon_0|^2$, and the ones for $\mu\neq\widehat{\mu}$ scale with $|\varepsilon_0|$ [see Eqs. (F5) and (F6)].

[1] A. Pasquazi, M. Peccianti, L. Razzari, D. J. Moss, S. Coen, M. Erkintalo, Y. K. Chembo, T. Hansson, S. Wabnitz, P. Del'Haye, X. Xue, A. M. Weiner, and R. Morandotti, Micro-combs: A novel generation of optical sources, Phys. Rep. **729**, 1 (2018).

[2] T. J. Kippenberg, A. L. Gaeta, M. Lipson, and M. Gorodetsky, Dissipative Kerr solitons in optical microresonators, Science **361**, eaan8083 (2018).

[3] V. S. Ilchenko, A. A. Savchenkov, A. B. Matsko, and L. Maleki, Nonlinear Optics And Crystalline Whispering Gallery Mode Cavities, Phys. Rev. Lett. **92**, 043903 (2004).

[4] J. U. Furst, D. V. Strekalov, D. Elser, M. Lassen, U. L. Andersen, C. Marquardt, and G. Leuchs, Naturally Phase-Matched Second Harmonic Generation In A Whispering-Gallery-Mode Resonator, Phys. Rev. Lett. **104**, 153901 (2010).

[5] J. U. Furst, D. V. Strekalov, D. Elser, A. Aiello, U. L. Andersen, Ch. Marquardt, and G. Leuchs, Low-Threshold Optical Parametric Oscillations In A Whispering Gallery Mode Resonator, Phys. Rev. Lett. **105**, 263904 (2010).

[6] T. Beckmann, H. Linnenbank, H. Steigerwald, B. Sturman, D. Haertle, K. Buse, and I. Breunig, Highly Tunable Low-Threshold Optical Parametric Oscillation In Radially Poled Whispering Gallery Resonators, Phys. Rev. Lett. **106**, 143903 (2011).

[7] I. Breunig, Three-wave mixing in whispering gallery resonators, Laser Photonics Rev. **10**, 569 (2016).

[8] M. Zhang, C. Wang, R. Cheng, A. Shams-Ansari, and M. Loncar, Monolithic ultra-high-Q lithium niobate microring resonator, Optica **4**, 1536 (2017).

[9] R. Wolf, Y. C. Jia, S. Bonaus, C. S. Werner, S. J. Herr, I. Breunig, K. Buse, and H. Zappe, Quasi-phase-matched nonlinear optical frequency conversion in on-chip whispering galleries, Optica **5**, 872 (2018).

[10] R. Ikuta, M. Asano, R. Tani, T. Yamamoto, and N. Imoto, Frequency comb generation in a quadratic nonlinear waveguide resonator, Opt. Exp. **26**, 15551 (2018).

[11] M. Stefszky, V. Ulvila, Z. Abdallah, C. Silberhorn, and M. Vainio, Towards optical-frequency-comb generation in continuous-wave-pumped titanium-indiffused lithium-niobate waveguide resonators, Phys. Rev. A **98**, 053850 (2018).

[12] J. Szabados, D. N. Puzyrev, Y. Minet, L. Reis, K. Buse, A. Villois, D. V. Skryabin, and I. Breunig, Frequency Comb Generation Via Cascaded Second-Order Nonlinearities In Microresonators, Phys. Rev. Lett. **124**, 203902 (2020).

[13] J. Szabados, B. Sturman, and I. Breunig, Frequency comb generation threshold via second-harmonic excitation in chi(2) optical microresonators, APL Photonics **5**, 116102 (2020).

[14] I. Hendry, L. S. Trainor, Y. Xu, S. Coen, S. G. Murdoch, H. G. Schwefel, and M. Erkintalo, Experimental observation of internally pumped parametric oscillation and quadratic comb generation in a chi((2)) whispering-gallery-mode microresonator, Opt. Lett. **45**, 1204 (2020).

[15] A. W. Bruch, X. Liu, Z. Gong, J. B. Surya, M. Li, C. L. Zou, and H. Tang, Pockels soliton microcomb, Nat. Photonics **15**, 21 (2021).

[16] S. Miller, K. Luke, Y. Okawachi, J. Cardenas, A. L. Gaeta, and M. Lipson, On-chip frequency comb generation at visible wavelengths via simultaneous second- and third-order optical nonlinearities, Opt. Exp. **22**, 26517 (2014).

[17] X. Xue, F. Leo, Y. Xuan, J. A. Jaramillo-Villegas, P.-H. Wang, D. E. Leaird, M. Erkintalo, M. Qi, and A. M. Weiner, Second-harmonic-assisted four-wave mixing in chip-based microresonator frequency comb generation, Light Sci. Appl. **6**, e16253 (2017).

[18] Y. He, Q.-F. Yang, J. Ling, R. Luo, H. Liang, M. Li, B. Shen, H. Wang, K. Vahala, and Q. Lin, A self-starting bi-chromatic $LiNbO_3$ soliton microcomb, Optica **6**, 1138 (2019).

[19] M. Yu, Y. Okawachi, R. Cheng, C. Wang, M. Zhang, A. L. Gaeta, and M. Loncar, Raman lasing and soliton mode-locking in lithium niobate microresonators, Light Sci. Appl. **9**, 9 (2020).

[20] X. Lu, G. Moille, A. Rao, D. A. Westly, and K. Srinivasan, Efficient photoinduced second-harmonic generation in silicon nitride photonics, Nat. Photonics **15**, 131 (2021).

[21] X. Guo, C. L. Zou, H. Jung, and H. X. Tang, On-Chip Strong Coupling And Efficient Frequency Conversion Between Telecom And Visible Optical Modes, Phys. Rev. Lett. **117**, 123902 (2016).

[22] J. Lu, M. Li, C. L. Zou, A. A. Sayem, and H. X. Tang, Toward 1% single-photon anharmonicity with periodically poled lithium niobate microring resonators, Optica **7**, 1654 (2020).

[23] D. V. Skryabin, V. V. Pankratov, A. Villois, and D. N. Puzyrev, Photon-photon polaritons in $\chi^{(2)}$ microresonators, Phys. Rev. Research **3**, L012017 (2021).

[24] I. Ricciardi, S. Mosca, M. Parisi, F. Leo, T. Hansson, M. Erkintalo, P. Maddaloni, P. De Natale, S. Wabnitz, and M. De Rosa, Optical frequency combs in quadratically nonlinear resonators, Micromachines **11**, 230 (2020).

[25] V. Ulvila and M. Vainio, Experimental study of the effect of phase mismatch on a CW-pumped cascaded quadratic nonlinear frequency comb, J. Phys. Photonics **2**, 034006 (2020).

[26] M. H. Dunn and M. Ebrahim-Zadeh, Parametric generation of tunable light from continuous-wave to femtosecond pulses, Science **286**, 1513 (1999).

[27] D. V. Skryabin and A. R. Champneys, Walking cavity solitons, Phys. Rev. E **63**, 066610 (2001).

[28] L. Torner, D. Mazilu, and D. Mihalache, Walking Solitons In Quadratic Nonlinear Media, Phys. Rev. Lett. **77**, 2455 (1996).

[29] D. V. Skryabin, Coupled-mode theory for microresonators with quadratic nonlinearity, J. Opt. Soc. Am. B **37**, 2604 (2020).

[30] A. Villois and D. V. Skryabin, Soliton and quasi-soliton frequency combs due to second harmonic generation in microresonators, Opt. Express **27**, 7098 (2019).

[31] A. Villois, N. Kondratiev, I. Breunig, D. N. Puzyrev, and D. V. Skryabin, Frequency combs in a microring optical parametric oscillator, Opt. Lett. **44**, 4443 (2019).

[32] R. Boyd, *Nonlinear Optics* (Academic, New York, 2008).

[33] R. C. Eckardt, C. D. Nabors, W. J. Kozlovsky, and R. L. Byer, Optical parametric oscillator frequency tuning and control, J. Opt. Soc. Am. B **8**, 646 (1991).

[34] S. Schiller and R. L. Byer, Quadruply resonant optical parametric oscillation in a monolithic total-internal-reflection resonator, J. Opt. Soc. Am. B **10**, 1696 (1993).

[35] D. V. Strekalov, A. S. Kowligy, V. G. Velev, G. S. Kanter, P. Kumar, and Y. Huang, Phase matching for the optical frequency conversion processes in whispering gallery mode resonators, J. Mod. Opt. **63**, 50 (2016).

[36] C. Schwob, P. F. Cohadon, C. Fabre, M. A. M. Marte, H. Ritsch, A. Gatti, and L. Lugiato, Transverse effects and mode couplings in OPOS, Appl. Phys. B **66**, 685 (1998).

[37] A. V. Buryak and Y. S. Kivshar, Solitons due to 2nd-harmonic generation, Phys. Lett. A **197**, 407 (1995).

[38] T. Hansson, P. Parra-Rivas, M. Bernard, F. Leo, L. Gelens, and S. Wabnitz, Quadratic soliton combs in doubly resonant second-harmonic generation, Opt. Lett. **43**, 6033 (2018).

[39] P. D. Drummond, K. J. McNeil, and D. F. Walls, Non-equilibrium transitions in sub/second harmonic generation, Opt. Acta **27**, 321 (1980).

[40] X. Guo, C. L. Zou, H. Jung, Z. Gong, A. Bruch, L. Jiang, and H. X. Tang, Efficient Generation of a Near-visible Frequency Comb via Cherenkov-like Radiation from a Kerr Microcomb, Phys. Rev. Appl. **10**, 014012 (2018).

[41] H. Suchowski, D. Oron, A. Arie, and Y. Silberberg, Geometrical representation of sum frequency generation and adiabatic frequency conversion, Phys. Rev. A **78**, 063821 (2008).

[42] I. Carusotto and G. C. La Rocca, Two-photon Rabi splitting and optical Stark effect in semiconductor microcavities, Phys. Rev. B **60**, 4907 (1999).

[43] A. Pikovsky, M. Rosenblum, and J. Kurths, *Synchronization: A Universal Concept in Nonlinear Sciences* (Cambridge University, Cambridge, England, 2001).

[44] The PDC conditions in Eq. (42) are the same as the four-wave-mixing ones, $\hbar\omega_p + \hbar\omega_p = \hbar\omega_{\mu\mathrm{f}}^{(j_1)} + \hbar\omega_{\mu\mathrm{f}}^{(j_2)}$, in Ref. [23].

[45] D. V. Skryabin, Z. Fan, A. Villois, and D. N. Puzyrev, Threshold of complexity and Arnold tongues in Kerr ring microresonators, Phys. Rev. A **103**, L011502 (2021).

[46] D. N. Puzyrev and D. V. Skryabin, Finesse and four-wave mixing in microresonators, Phys. Rev. A **103**, 013508 (2021).

[47] D. V. Skryabin and Y. V. Kartashov, Self-locking of the frequency comb repetition rate in microring resonators with higher order dispersions, Opt. Express **25**, 27442 (2017).

[48] C. Kittel, *Introduction to Solid State Physics* (Wiley, New York, 1996).

[49] P. Parra-Rivas, D. Gomila, L. Gelens, and E. Knobloch, Bifurcation structure of periodic patterns in the Lugiato-Lefever equation with anomalous dispersion, Phys. Rev. E **98**, 042212 (2018).

[50] A. Coillet, I. Balakireva, R. Henriet, K. Saleh, L. Larger, J. M. Dudley, C. R. Menyuk, and Y. K. Chembo, Azimuthal turing patterns, bright and dark cavity solitons in kerr combs generated with whispering-gallery-mode resonators, IEEE Photonics J. **5**, 6100409 (2013).

[51] Z. Qi, S. Wang, J. Jaramillo-Villegas, M. H. Qi, A. M. Weiner, G. D'Aguanno, T. F. Carruthers, and C. R. Menyuk, Dissipative cnoidal waves (Turing rolls) and the soliton limit in microring resonators, Optica **6**, 1220 (2019).

[52] G. L. Oppo, M. Brambilla, and L. A. Lugiato, Formation and evolution of roll patterns in optical parametric oscillators, Phys. Rev. A **49**, 2028 (1994).

[53] G. J. de Valcarcel, K. Staliunas, E. Roldan, and V. J. Sanchez-Morcillo, Transverse patterns in degenerate optical parametric oscillation and degenerate four-wave mixing, Phys. Rev. A **54**, 1609 (1996).

[54] S. Longhi, Traveling-wave states and secondary instabilities in optical parametric oscillators, Phys. Rev. A **53**, 4488 (1996).

[55] C. Etrich, U. Peschel, and F. Lederer, Solitary Waves In Quadratically Nonlinear Resonators, Phys. Rev. Lett. **79**, 2454 (1997).

[56] M. Santagiustina, P. Colet, M. San Miguel, and D. Walgraef, Walk-off and pattern selection in optical parametric oscillators, Opt. Lett. **23**, 1167 (1998).

[57] P. Lodahl and M. Saffman, Pattern formation in singly resonant second-harmonic generation with competing parametric oscillation, Phys. Rev. A **60**, 3251 (1999).

[58] D. V. Skryabin, Instabilities of cavity solitons in optical parametric oscillators, Phys. Rev. E **60**, R3508 (1999).

[59] A. Coillet, J. Dudley, G. Genty, L. Larger, and Y. K. Chembo, Optical rogue waves in whispering-gallery-mode resonators, Phys. Rev. A **89**, 013835 (2014).

[60] S. W. Huang, H. Zhou, J. Yang, J. F. McMillan, A. Matsko, M. Yu, D. L. Kwong, L. Maleki, and C. W. Wong, Mode-Locked Ultrashort Pulse Generation From On-Chip Normal Dispersion Microresonators, Phys. Rev. Lett. **114**, 053901 (2015).

[61] S. Coulibaly, M. Taki, A. Bendahmane, G. Millot, B. Kibler, and M. G. Clerc, Turbulence-Induced Rogue Waves In Kerr Resonators, Phys. Rev. X **9**, 011054 (2019).

[62] C. Milian and D. V. Skryabin, Soliton families and resonant radiation in a micro-ring resonator near zero group-velocity dispersion, Opt. Express **22**, 3732 (2014).

[63] V. Brasch, M. Geiselmann, T. Herr, G. Lihachev, M. H. P. Pfeiffer, M. L. Gorodetsky, and T. J. Kippenberg, Photonic chip-based optical frequency comb using soliton Cherenkov radiation, Science **351**, 357 (2016).

[64] D. V. Skryabin and A. V. Gorbach, Colloquium: Looking at a soliton through the prism of optical supercontinuum, Rev. Mod. Phys. **82**, 1287 (2010).

[65] M. Bache, O. Bang, B. B. Zhou, J. Moses, and F. W. Wise, Optical Cherenkov radiation by cascaded nonlinear interaction: An efficient source of few-cycle energetic near- to mid-IR pulses, Opt. Express **19**, 22557 (2011).

[66] M. Jankowski, A. Marandi, C. R. Phillips, R. Hamerly, K. A. Ingold, R. L. Byer, and M. M. Fejer, Temporal Simultons In Optical Parametric Oscillators, Phys. Rev. Lett. **120**, 053904 (2018).

[67] P. Parra-Rivas, L. Gelens, T. Hansson, S. Wabnitz, and F. Leo, Frequency comb generation through the locking of domain walls in doubly resonant dispersive optical parametric oscillators, Opt. Lett. **44**, 2004 (2019).

[68] V. E. Lobanov, Two-color flat-top solitons in microresonator-based optical parametric oscillators, Phys. Rev. A **102**, 013518 (2020).

[69] E. Podivilov, S. Smirnov, I. Breunig, and B. Sturman, Nonlinear solutions for chi(2) frequency combs in optical microresonators, Phys. Rev. A **101**, 023815 (2020).

[70] D. V. Skryabin, Instabilities of vortices in a binary mixture of trapped Bose-Einstein condensates: Role of collective excitations with positive and negative energies, Phys. Rev. A **63**, 013602 (2000).